Structures 39 (2022) 175–193

Contents lists available at ScienceDirect

Structures

journal homepage: www.elsevier.com/locate/structures

Ultimate response and plastic design of aluminium alloy continuous beams

Evangelia Georgantzia *, Michaela Gkantou, George S. Kamaris, Kunal D. Kansara

School of Civil Engineering and Built Environment, Liverpool John Moores University, United Kingdom

ARTICLE INFO

Keywords:
Aluminium
Tubular
Continuous beams
Finite Element
Plastic design
Eurocode 9
Continuous strength method (CSM)
Plastic hinge method

ABSTRACT

Over the last twenty years 6,000 series aluminium alloys are gaining increasing attention as a structural material in the construction sector, particularly in applications where lightness and corrosion resistance are crucial for material selection. Aiming to sustainable construction practices, significant material savings could be achieved through more economical design solutions such as plastic design. Currently, plastic design of aluminium alloy structures is not permitted in most design codes, except European provisions which provide recommendations for inelastic analysis. Indeed, there is a clear lack of experimental data to prove this possibility, particularly for relatively new materials in the construction industry, such as the 6082-T6 heat-treated aluminium alloy. To address this knowledge gap, a total of 15 rectangular hollow sections fabricated from 6082-T6 aluminium alloy were tested as simply-supported and two-span continuous beams. Numerical models were developed to replicate the experimental results considering geometric and material nonlinearities. A subsequent parametric study was carried out to generate numerical data for indeterminate structures. One normal and two high strength aluminium alloys as well as two load configurations were examined within this parametric study over a wide range of cross-sectional aspect ratios and slendernesses. The experimental results in combination with the numerical results were utilised to assess the accuracy and applicability of (i) the traditional plastic design method, (ii) the European design provisions (EC9), (iii) the plastic hinge method included in Annex H of EC9, and (iv) the Continuous Strength Method (CSM). Relative comparisons demonstrated the potential of applying plastic design in aluminium alloy indeterminate structures. Notably, the plastic hinge method and the CSM which accounts for strain hardening at the cross-sectional level and for moment redistribution at the system level were found to provide the most accurate design strength predictions, resulting in more economical cross-sections and utilising the full potential of aluminium alloys' plastic deformability.

1. Introduction

The excellent corrosion resistance and high strength-to-weight ratios, along with advantageous mechanical properties of 6,000 series aluminium alloys make them great alternatives to steel in structural applications. Even though aluminium alloys may have less ductility compared to steel, they may still have sufficient rotational capacity allowing for moment redistribution and thereby the application of plastic design concept [1]. Continuity in a structural system provides attractive benefits, such as increased load-carrying capacity and decreased deflection for a given cross-section or employment of more economical cross-sections for given loading and deflection limits [1]. It is noteworthy that research work on stainless steel continuous beams demonstrated that considering moment redistribution during design could enhance the design capacity up to 10% [2] and provide a more accurate prediction of the structural response [3].

Design guidance for aluminium alloy structural elements is provided by a number of international design codes [4–6]. However, their design framework is based on limited research work and sometimes it adopts the same principles to their steel counterparts without considering the main differences between the two materials. This fact results in rather conservative predictions which are opposed to an efficient design philosophy from an economical point of view [7]. Currently, plastic design of aluminium alloy structures is not permitted according to Aluminum Design Manual [4] and the Australian and New Zealand Standards [5]. Eurocode 9 (EC9) [6] is the first design code which allows for complete inelastic analysis [8] including the plastic hinge method in Annex H as an alternative approach for indeterminate beams with Class 1 cross-sections considering moment redistribution and material strain hardening. A series of reported works on aluminium alloy members [9–16] demonstrated the influence of strain hardening on the ultimate strength and the necessity to be considered by the design codes in order to

* Corresponding author.
E-mail address: E.Georgantzia@2019.ljmu.ac.uk (E. Georgantzia).

https://doi.org/10.1016/j.istruc.2022.03.015
Received 18 October 2021; Received in revised form 14 February 2022; Accepted 5 March 2022
Available online 15 March 2022

improve design efficiency.

To date, there are limited reported studies on the inelastic behaviour of indeterminate aluminium alloy structures. Panlilo [17] conducted tests on two-span beams, whereas Welo [18] investigated 18 simply-supported and three-span continuous beams to verify the applicability of the existing plastic hinge methods on structural aluminium alloys. Based on the resulting test data of the latter, Manganiello et al. [19] carried out an extensive numerical study to determine the required rotational capacity allowing for adequate moment redistribution in case of continuous beams and framed structures. More recently, Su et al. [15,20] assessed the ultimate response of two-span continuous beams with square and rectangular hollow sections (SHSs/RHSs) fabricated from 6061-T6 and 6063-T5 heat-treated aluminium alloys. On the basis of the experimental findings, they modified the Continuous Strength Method (CSM) [21], originally proposed for indeterminate stainless steel beams, to cover aluminium alloy structures. The CSM for indeterminate structures is a deformation-based design approach which utilises the merits of the traditional plastic analysis in combination with an accurate evaluation of the cross-sectional bending moment capacity accounting for a systematic exploitation of strain hardening. Comparing the tests results obtained from [16,20] with the ultimate strengths calculated according to [4–6] and CSM, it was concluded that the CSM provides more precise and consistent design predictions. However, the existing literature data are insufficient and thus there is a need of further investigation on the inelastic response of aluminium alloy indeterminate structures.

To date, there are scarce studies (four publications, i.e., [17–20]) that examine the potential of plastic design of aluminium alloys. As also recommended in the conclusions of the most recent relevant publication [20], there is a need of further investigation on the inelastic response of aluminium alloy indeterminate structures. Indeed, even though EC9 allows inelastic analysis, there is a clear lack of experimental data to prove this possibility, particularly for relatively new materials in the construction industry, such as the 6082-T6 heat-treated aluminium alloy. 6082-T6 along with 6061-T6 belong to the aluminium-magnesium-silicon family (6,000 series), which is favourable for structural applications due to its strength. 6061-T6 is predominantly produced for the American market, whilst 6082-T6 is the nearest equivalent alloy that is readily available in the UK. However, they have different composition ratios of silicon and magnesium which makes 6082-T6 slightly stronger and more brittle than 6061-T6 [1]. Since 6082-T6 is the regular stock material in Europe and is less ductile than 6061-T6 which has already been investigated [15,20], this study was deemed necessary to examine whether 6082-T6 may still have sufficient rotational capacity allowing the application of plastic design concept.

The present paper examines the potential of applying plastic design to 6082-T6 aluminium alloy structures. An experimental investigation on 5 two-span RHS continuous beams is reported. Additional tests on simply-supported beams with the same cross-sections were performed to determine the flexural response under moment gradient (three-point bending tests) and uniform bending moment (four-point bending tests). The relatively new 6082-T6 heat-treated aluminium alloy, whose potential for plastic design has not been previously investigated, is examined herein. This alloy is favourable for structural applications due to its strength, which is the highest amongst the 6,000 series alloys. The mechanical properties of 6082-T6 aluminium alloy were determined through tensile coupon tests and were utilised to develop finite element (FE) models. Upon successfully validating the FE models based on the experimental data, a comprehensive parametric study was conducted to extend the pool of performance data on the structural response of aluminium alloy indeterminate structures. The experimentally and numerically obtained ultimate strengths were utilised to assess the accuracy and applicability of international design specifications and methods, viz.: (i) the traditional plastic design method, (ii) the European design standard (EC9) [6], (iii) the plastic hinge method included in Annex H of EC9 [6], and (iv) the CSM.

2. Experimental programme

In order to examine the structural performance of indeterminate aluminium alloy structures, a series of tests was performed in the Light Structures and Materials Laboratory of the School of Civil Engineering and Built Environment at Liverpool John Moores University. Simply-supported RHS beams were investigated under three-point and four-point bending configuration to capture their flexural response and obtain their rotational capacity. Subsequently, the same cross-sections were tested as two-span continuous beams (five-point bending configuration) to investigate the moment redistribution and capture the ultimate strengths. Moreover, tensile tests were conducted on flat coupons extracted from each test specimen to determine the material properties of the examined 6082-T6 heat-treated aluminium alloy.

2.1. Test specimens and geometric imperfection measurements

The experimental investigation comprised five 6082-T6 RHSs with geometric properties as shown in Fig. 1. Since the objective of this study is to explore the possibility of plastic design in aluminium alloy indeterminate structures, the examined cross-sections were chosen to be Class 1, i.e., capable of developing their collapse resistance without presence of local instabilities, according to EC9 [6]. The beam specimens for each cross-section were cut from the same tube and their geometric measured dimensions are presented in Table 1, where D is the outer web depth, B is the outer flange width and t is the thickness. The specimens designation is defined according to their nominal geometric dimensions.

The initial geometric imperfections inherently present in metallic structural members may have significant impact on their structural response and thus they should be measured prior to testing. In the current study, only the local geometric imperfections were measured because the investigated cross-sections have closed shape and short length, precluding the occurrence of lateral-torsional buckling. The measurements were carefully executed using a linear height gauge machine. Measuring points were defined at 20 mm intervals along a centreline inscribed over the entire length on each of the four faces of the beam specimens. For each face, the recorded values were used to determine the maximum deviation from a flat datum, and the maximum value amongst the four faces was reported as the local imperfection amplitude of the beam specimen. The measured local imperfection amplitudes denoted ω_l are reported in Table 1.

2.2. Aluminium 6082-T6: Tensile coupon tests

Material tensile coupon tests were performed following the procedure outlined in EN ISO 6892-1 [22] to determine the engineering stress–strain (σ-ε) response of the examined 6082-T6 heat-treated aluminium alloy. For each employed tubular cross-section, two flat coupons; one from the mid-width of the web and one of the mid-width of

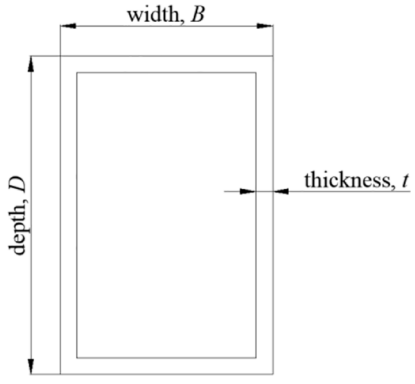

Fig. 1. Geometric properties of tested cross-sections.

Table 1
Mean measured dimensions and local geometric imperfections of tested cross-sections.

Specimen	D (mm)	B (mm)	t (mm)	ω_l (mm)
Three-point bending				
63.5 × 38.1 × 3.25	63.32	37.98	3.22	0.25 (t/13)
50.8 × 38.1 × 3.25	50.96	38.27	3.41	0.18 (t/19)
50.8 × 25.4 × 3.25	50.83	25.46	3.31	0.19 (t/17)
38.1 × 25.4 × 3.25	38.11	25.33	3.20	0.21 (t/15)
38.1 × 19.1 × 3.25	38.07	19.05	3.28	0.32 (t/10)
Four-point bending				
63.5 × 38.1 × 3.25	63.35	37.99	3.20	0.27 (t/12)
50.8 × 38.1 × 3.25	50.93	38.24	3.39	0.33 (t/10)
50.8 × 25.4 × 3.25	50.82	25.47	3.33	0.16 (t/21)
38.1 × 25.4 × 3.25	38.14	25.85	3.23	0.18 (t/18)
38.1 × 19.1 × 3.25	38.17	19.05	3.24	0.21 (t/15)
Two-span continuous beams				
63.5 × 38.1 × 3.25	63.57	38.04	3.25	0.21 (t/15)
50.8 × 38.1 × 3.25	50.99	38.30	3.45	0.14 (t/24)
50.8 × 25.4 × 3.25	51.15	25.48	3.36	0.20 (t/16)
38.1 × 25.4 × 3.25	38.22	25.47	3.31	0.17 (t/19)
38.1 × 19.1 × 3.25	38.11	19.05	3.37	0.50 (t/7)

the flange were cut with a nominal width of 12 mm and gauge length of 100 mm. Afterwards, the coupons were placed between the jaws of a 50 kN Tinius Olsen testing machine and were loaded with 0.2 mm/min displacement rate up to fracture. Moreover, a calibrated extensometer was attached onto the mid-length of the coupon specimens to measure the longitudinal strains during testing. Table 2 summarises the mean values of the obtained key results, namely the initial modulus of elasticity E, the 0.1 % proof stress $\sigma_{0.1}$, the 0.2 % proof stress $\sigma_{0.2}$, the ultimate tensile stress σ_u, the strain at fracture ε_f and the strain hardening exponent n based on the material model proposed by Ramberg and Osgood [23] and modified by Hill [24]. Note that the obtained results will be utilised in the following numerical study.

Fig. 2 illustrates the stress–strain curves for all specimens obtained from the tensile coupon tests. As can be seen, the investigated 6082-T6 aluminium alloy exhibits a round stress–strain behaviour without a clearly defined yield point due to continuous strain hardening. The strain hardening ratio $\sigma_u/\sigma_{0.2}$ for each examined cross-section is, also, included in Table 2, reaching up to 14%. Moreover, Fig. 3 displays the tensile coupons before and after testing.

2.3. Simply-supported beam tests

A total of ten symmetric bending tests on simply-supported beams were performed aiming to quantify the moment resistance and rotational capacity of each examined cross-section. Three-point and four-point bending configurations were adopted to explore the cross-sectional response under moment gradient and constant moment, respectively. The considered cross-sections were tested under in-plane bending about the major axis. Schematic illustrations of the three- and four-point test arrangements along with the corresponding employed instrumentations are depicted in Figs. 4 and 5, respectively. The investigated beam specimens had a total length of 1000 mm and overhung each end by 50 mm beyond the centerlines of the supports, resulting in a

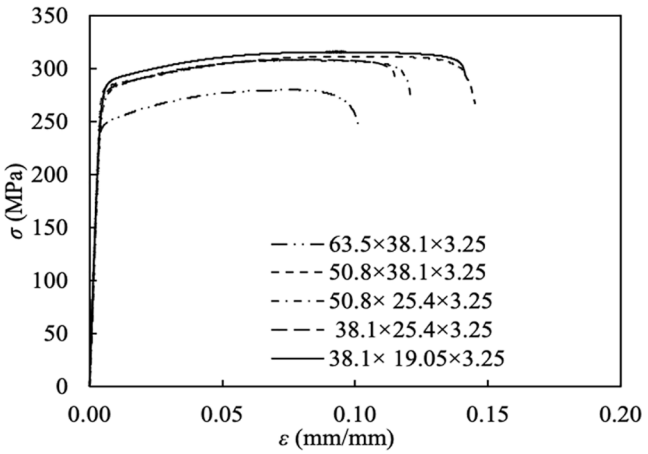

Fig. 2. Stress–strain curves obtained from the tensile coupon tests.

clear beam span of 900 mm. The span-to-height ratio ranged from 14 to 23 representing the proportions of actual beams and sufficiently high to preclude any shear dominance on the flexural response [25]. The simply-supported boundary conditions were elaborated using steel rollers which allowed free rotation about the major axis as well as free longitudinal displacement of the specimen's ends. In order to prevent the occurrence of web crippling due to localised stress concentration, wooden blocks with dimensions equal to the internal ones of the tested cross-sections were inserted within the tubes at the loading points and supports. A Mayes servo-controlled hydraulic testing machine with 600 kN capacity was used to apply load at 0.8 mm/min cross-head displacement rate. The load was applied symmetrically at mid-span in three-point bending tests and at third-points in four-point bending tests via a spreader beam located between the two steel rollers and the hydraulic jack of the machine.

Linear electrical resistance strain gauges were attached to top and bottom flanges of each cross-section and at 50 mm distance from the mid-span to measure the extreme compressive and tensile strains during testing. In addition, in three-point bending tests, as shown in Fig. 6, one linear variable displacement transducer (LVDT) was located at the mid-span to record the vertical displacement, whilst two inclinometers were positioned at the support locations to measure the end rotations. In four-point bending tests, as shown in Fig. 7, three LVDTs were attached at both mid-span and loading points to monitor the vertical displacements and determine the curvature in the constant moment area. The applied load, strains, displacements and end rotations were recorded using a data acquisition system at 2 s intervals.

The moment-rotation and moment–curvature responses obtained from the three-point and four-point bending tests, respectively, are depicted in Figs. 8 and 9, respectively. For comparison purposes, the curves are plotted in a non-dimensional format. Thus, the recorded moment M is normalised by the plastic moment resistance M_{pl}, while the rotation θ at the plastic hinge (sum of the two end rotation values measured from the inclinometers) or curvature κ at the constant moment area is normalised by θ_{pl} or κ_{pl} which is the elastic component of the rotation or curvature corresponding to M_{pl}. The terms θ_{pl} and κ_{pl} are defined in Eqs. (1) and (2), respectively:.

Table 2
Material properties obtained from the tensile coupon tests.

Specimen	E (MPa)	$\sigma_{0.1}$ (MPa)	$\sigma_{0.2}$ (MPa)	σ_u (MPa)	ε_u (mm/mm)	ε_f (mm/mm)	n	$\sigma_u/\sigma_{0.2}$
63.5 × 38.1 × 3.25	70,962	242	247	280	0.08	0.10	33.89	1.13
50.8 × 38.1 × 3.25	67,925	275	282	311	0.11	0.13	27.58	1.10
50.8 × 25.4 × 3.25	66,280	264	271	308	0.08	0.12	26.49	1.14
38.1 × 25.4 × 3.25	67,123	271	278	308	0.08	0.11	29.24	1.11
38.1 × 19.1 × 3.25	70,302	275	282	316	0.09	0.14	27.58	1.12

Fig. 3. Tensile coupons.

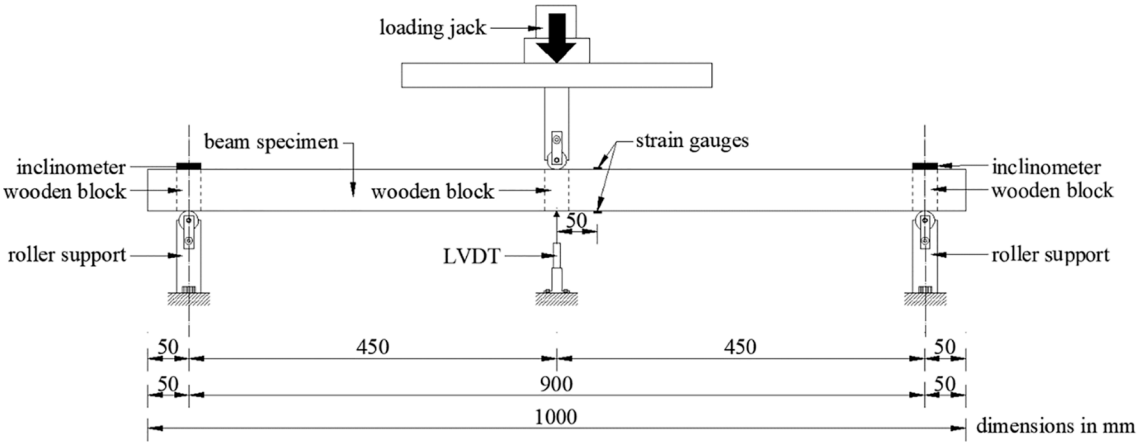

Fig. 4. Schematic illustration of the three-point bending test arrangement and instrumentation.

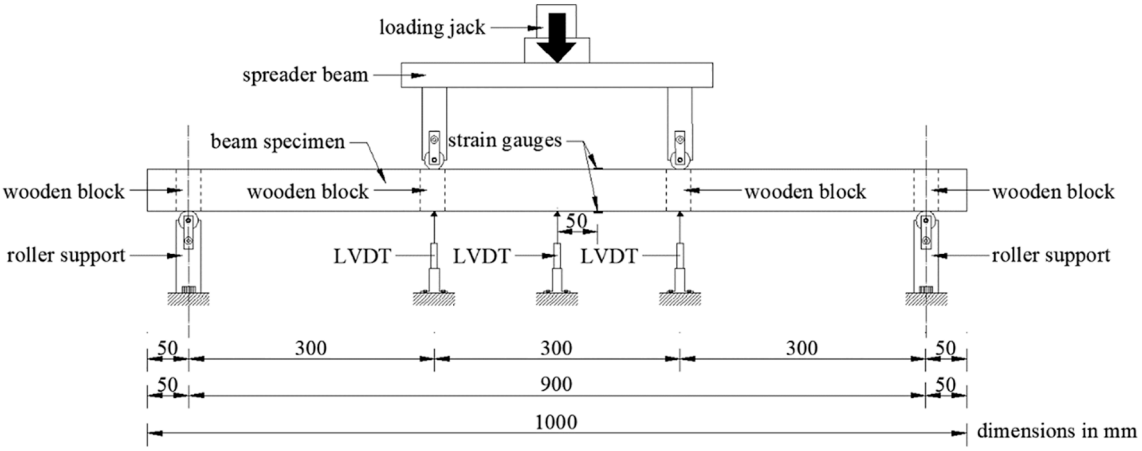

Fig. 5. Schematic illustration of the four-point bending test arrangement and instrumentation.

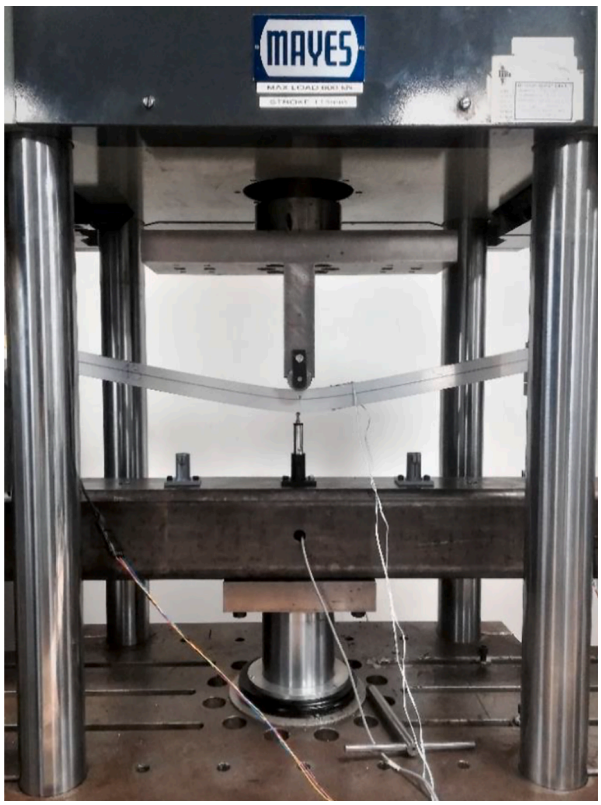

Fig. 6. Typical three-point bending test set-up.

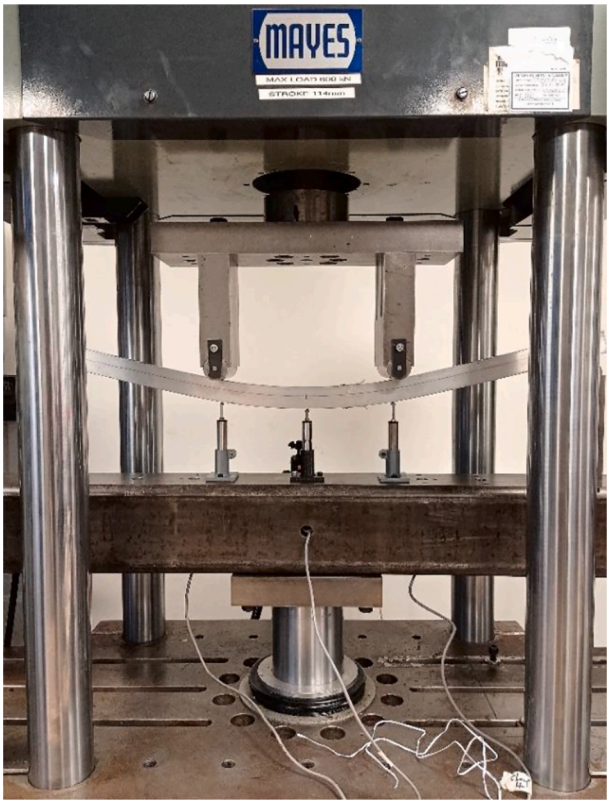

Fig. 7. Typical four-point bending test set-up.

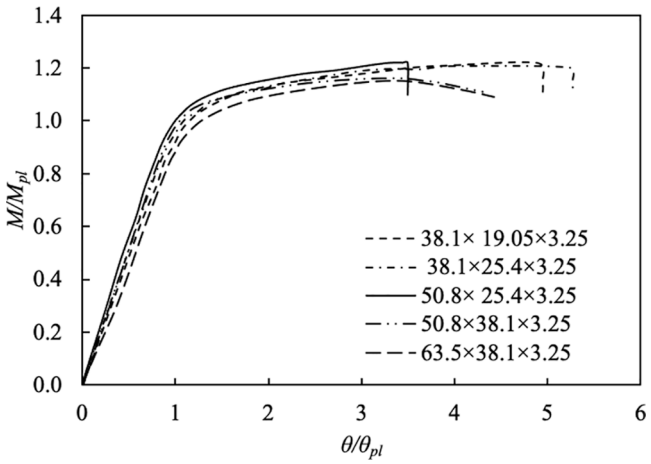

Fig. 8. Normalised moment-rotation responses obtained from three-point bending tests.

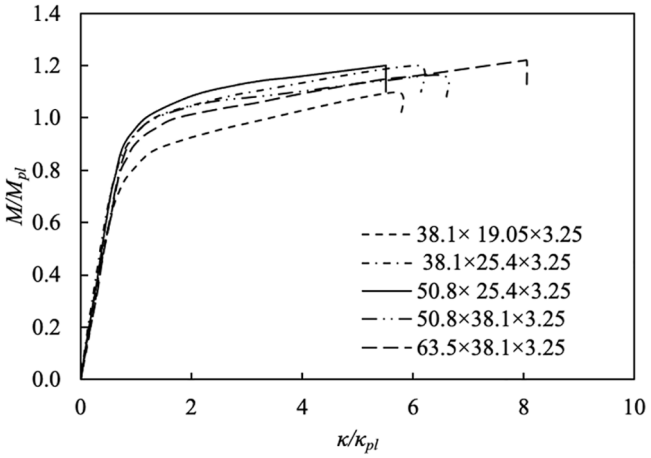

Fig. 9. Normalised moment–curvature responses obtained from four-point bending tests.

$$\theta_{pl} = \frac{M_{pl}L}{2EI} \tag{1}$$

$$\kappa_{pl} = \frac{M_{pl}}{EI} \tag{2}$$

where the plastic moment resistance M_{pl} is calculated by multiplying the 0.2 % proof (yield) stress obtained from the tensile coupon tests by the plastic section modulus; L is the clear span of the beam specimen; E is the modulus of elasticity; and I is the second moment of inertia of the cross-section about the major axis.

In four-point bending tests the curvature κ in the constant moment area of the beam was determined using Eq. (3) considering that the deformed shape of the central span of length L_2 represents a segment of a circular arc of radius r [26].

$$\kappa = \frac{1}{r} = \frac{8(\delta_M - \delta_L)}{4(\delta_M - \delta_L)^2 + L_2^2} \tag{3}$$

where δ_M is the mid-span vertical displacement and δ_L is the average vertical displacement taken at the two loading points.

As shown from Figs. 8 and 9, all specimens at the initial loading stage exhibit a linear response. As the loading increases, the specimens exceed their plastic moment resistance and maintain it throughout large inelastic deformations denoting high deformation capacity. It is noteworthy that the specimens under four-point bending configuration

Table 3
Experimental results obtained from three-point and four-point bending tests.

Specimen	M_{el} (kNm)	M_{pl} (kNm)	M_{pl}/M_{el}	$M_{u,Exp}$ (kNm)	$M_{u,Exp}/M_{el}$	$M_{u,Exp}/M_{pl}$	θ_m/θ_{pl}	κ_m/κ_{pl}	R_m
Three-point bending									
63.5 × 38.1 × 3.25	2.53	3.15	1.24	3.57	1.41	1.13	4.42	–	3.42
50.8 × 38.1 × 3.25	2.20	2.72	1.24	3.12	1.42	1.15	4.30	–	3.30
50.8 × 25.4 × 3.25	1.56	2.01	1.29	2.39	1.53	1.19	3.50	–	2.50
38.1 × 25.4 × 3.25	1.00	1.28	1.27	1.49	1.49	1.17	5.27	–	4.27
38.1 × 19.1 × 3.25	0.83	1.10	1.32	1.31	1.57	1.19	4.95	–	3.95
Four-point bending									
63.5 × 38.1 × 3.25	2.53	3.15	1.24	3.77	1.49	1.20	–	8.05	7.05
50.8 × 38.1 × 3.25	2.20	2.72	1.24	3.10	1.41	1.14	–	6.60	5.60
50.8 × 25.4 × 3.25	1.56	2.01	1.29	2.36	1.52	1.18	–	5.51	4.51
38.1 × 25.4 × 3.25	1.00	1.28	1.27	1.49	1.49	1.17	–	6.15	5.15
38.1 × 19.1 × 3.25	0.83	1.10	1.32	1.18	1.42	1.08	–	5.75	4.75

possess higher deformation capacity, as they reached larger inelastic deformations.

The key response characteristics including the ultimate bending moment $M_{u,Exp}$, which is the maximum bending moment recorded during testing, the elastic moment resistance M_{el} and the plastic moment resistance M_{pl} are listed in Table 3. The obtained normalised rotation θ_m/θ_{pl} and curvature κ_m/κ_{pl} for each beam specimen, where θ_m (κ_m) is the rotation (curvature) value corresponding to bending moment $M_{u,Exp}$, are also reported. Note that some tests were discontinued before reaching the full moment–rotation/curvature potential due to either limited vertical displacement capacity of the test rig or excessive vertical deflection of the beam specimen. In these cases, the maximum recorded moment and rotation/curvature values are reported. On the basis of the recorded moment-rotation and moment–curvature responses, the rotational capacity R_m of the tested beam specimens under three-point and four-point cases was defined using the Eqs. (4) and (5), respectively, and are listed in Table 3.

$$R_m = \frac{\theta_m}{\theta_{pl}} - 1 \tag{4}$$

$$R_m = \frac{\kappa_m}{\kappa_{pl}} - 1 \tag{5}$$

Further comparisons on the responses exhibited by the cross-sections under three-point and four-point bending denoted a clear influence of the moment gradient on the ultimate bending moment and rotational capacity. This influence can be observed in Table 3 where in almost all cases the moment gradient allow the cross-section to sustain slightly higher loading. This behaviour which has also been observed in similar studies [14,26–31] stems from the fact that in three-point bending configuration the material surrounding the plastic hinge is stiffer and at lower stress providing a kind of restraint which delays the occurrence of local buckling.

Almost all beam specimens subjected to three-point and four-point major axis bending failed by material yielding, as shown in Figs. 10 and 11(a). In specimen 63.5 × 38.1 × 3.25 under both bending configurations, material yielding was accompanied with pronounced inelastic local buckling of the compression flange and the upper part of the web (Fig. 11(b)). It is also noteworthy that the specimen 50.8 × 25.4 × 3.25 under three-point bending configuration failed by material fracture at the tension flange at the mid-span, due to exceedance of the material fracture strain ε_f (Fig. 11(c)).

2.4. Continuous beams tests

Aiming to estimate the rotational capacity and the potential for moment redistribution of aluminium alloy indeterminate beams, the cross-sections employed for the simply-supported beam tests were subjected to five-point bending. A total of five two-span continuous beams were tested with a total length of 2000 mm. Each specimen overhung each end by 100 mm beyond the centerlines of the supports resulting in a clear beam span of 900 mm. Fig. 12 illustrates a schematic view of the test arrangement and the corresponding employed instrumentation. The support conditions were formed using steel rollers, whilst wooden blocks were inserted into the tubular specimens at the loading points and the supports to prevent web crippling occurrence. The load was applied through a hydraulic testing machine at 0.8 mm/min cross-head displacement rate. The beams were loaded symmetrically at both mid-spans using a spreader beam placed between the two steel rollers and the hydraulic jack of the machine.

The employed instrumentation consisted of four load cells located at the supports and underneath the ram of the hydraulic jack to measure the reaction forces (unknown due to statical indeterminacy) and the overall applied loading, respectively. Two LVDTs were also placed at both mid-spans to monitor the corresponding vertical displacements. Two inclinometers were attached to the end supports and two additional to the either side of the central support to record the rotations during

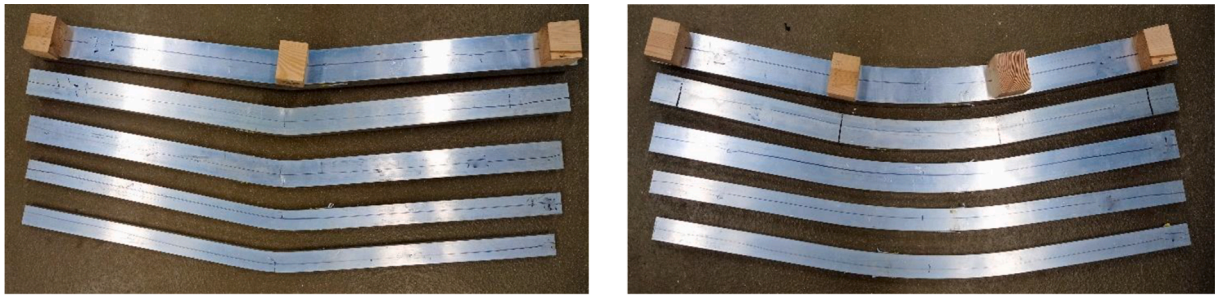

Fig. 10. Failure modes obtained from three-point and four-point bending tests.

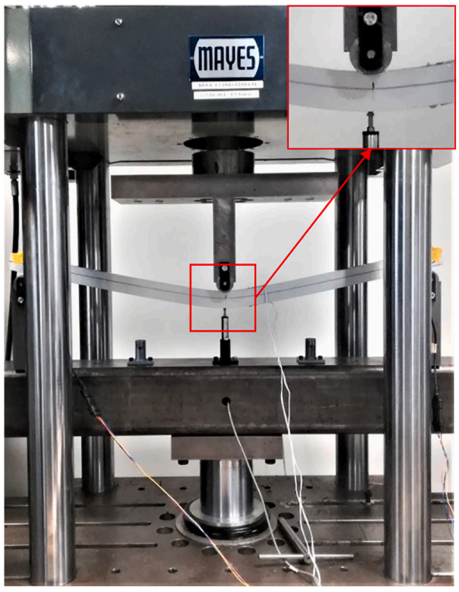

(a) Material yielding of 38.1×25.4×3.25 specimen

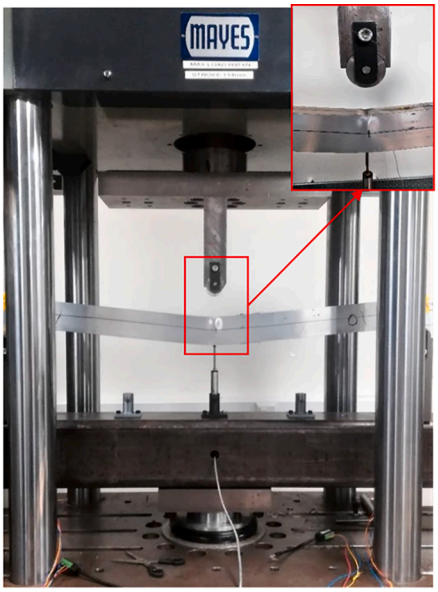

(b) Material yielding and inelastic local buckling of 63.5×38.1×3.25 specimen

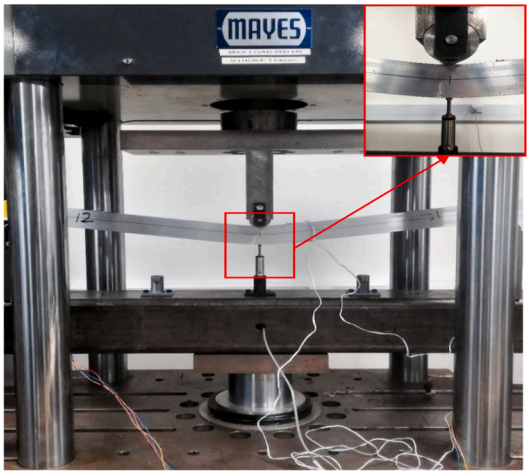

(c) Tensile fracture of 50.8×25.4×3.25 specimen

Fig. 11. Failure modes obtained from three-point bending tests.

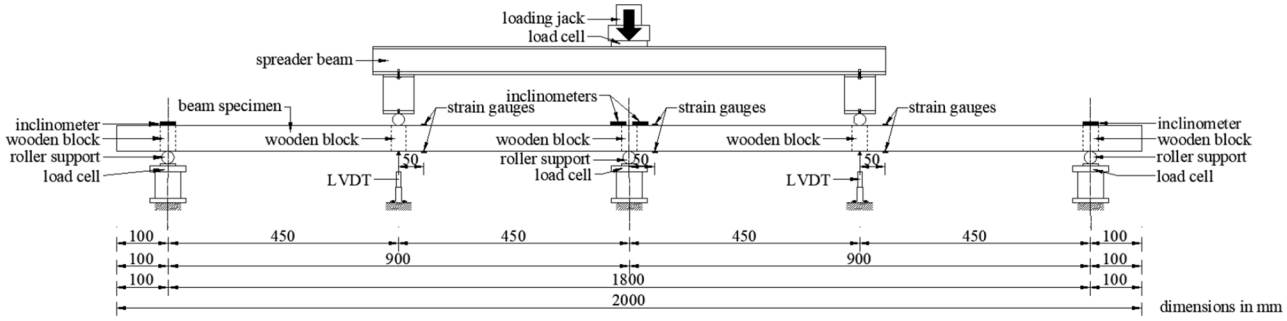

Fig. 12. Schematic illustration of the continuous beam test arrangement and instrumentation.

testing. Furthermore, six linear electrical resistance strain gauges were affixed to the top and bottom flange of the cross-section at 50 mm distance from the loading points and the central supports, as shown in Fig. 12, to ensure that the end rollers did not provide any axial restraint. A photograph of the overall set-up is displayed in Fig. 13. The applied load, reaction forces, strains, displacements and end rotations were all

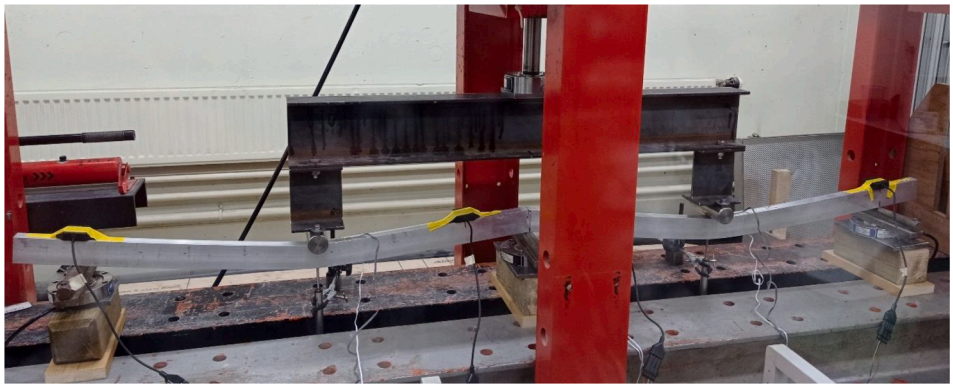

Fig. 13. Typical continuous beam test set-up.

Table 4
Experimental results obtained from continuous beam tests.

Specimen	$F_{u,Exp}$ [kN]	F_{coll} [kN]	δ_u [mm]	θ_u [deg]
63.5 × 38.1 × 3.25	43.98	42.01	18.60	3.95
50.8 × 38.1 × 3.25	39.38	36.26	48.53	7.89
50.8 × 25.4 × 3.25	30.70	26.76	36.99	6.60
38.1 × 25.4 × 3.25	19.80	17.01	66.16	11.20
38.1 × 19.1 × 3.25	17.20	14.63	61.92	9.45

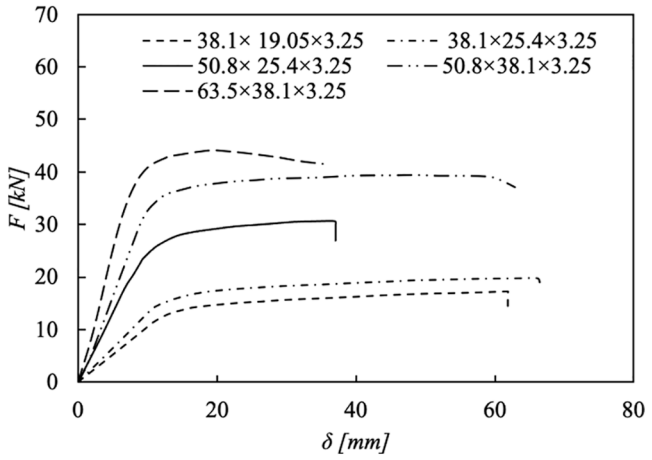

Fig. 14. Load-displacement responses obtained from continuous beam tests.

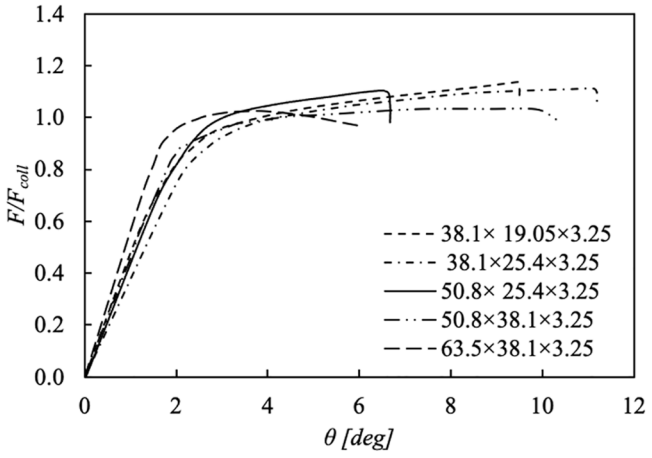

Fig. 15. Normalised load-end-rotation responses obtained from continuous beam tests.

recorded using a data acquisition system at 2 s intervals.

The test key response characteristics are summarised in Table 4, where $F_{u,Exp}$ is the ultimate load at collapse stage, δ_u is the mid-span vertical displacement at collapse stage, taken as average value of both LVDTs, and θ_u is the end-rotation at collapse stage, arisen in the most heavily stressed cross-section. In the same table, the theoretical collapse load F_{coll} which was determined using classical plastic analysis theory, is also reported. The experimental response for each tested beam specimen is depicted in Fig. 14, where the applied load is plotted against the average measured mid-span vertical displacement δ. Moreover, in Fig. 15, the applied load normalised by the theoretical collapse load F_{coll} is plotted against the average measured end rotation θ. According to the obtained curves plotted in Figs. 14 and 15, all specimens initially exhibit a linear response. Following, they exceed their plastic moment resistance and almost all (except from 63.5 × 38.1 × 3.25 specimen) maintain it throughout large inelastic deformations denoting high deformation capacity.

The observed failure mechanism of all the investigated specimens consisted of three distinct plastic hinges. As was expected the first plastic hinge was formed at the central support which was the most heavily stressed cross-section. Further spread of plasticity and moment redistribution occurrence resulted in two additional plastic hinges at both loading points, as shown in Fig. 16. Fig. 17 presents the evolution of the M_{sup}/M_{span} ratio with increasing average vertical displacement for the 63.5 × 38.1 × 3.25 and 50.8 × 38.1 × 3.25 specimens. The M_{sup}/M_{span} ratio corresponds to the experimental bending moment of the central support over the bending moment of the mid-span. This ratio is utilised to evaluate whether the theoretical response based on elastic-perfectly plastic analysis is in line with the experimental response. In Fig. 17, the horizontal lines of 1.2 and 1.0 which correspond to the theoretical moment ratios derived from elastic and rigid plastic analysis, respectively, are also included. As can be observed, the initial experimental moment ratio is equal to the theoretical moment ratio evaluated from elastic analysis (i.e., horizontal line of the elastic limit). For increasing deformation, the experimental moment ratio shifts towards the theoretical plastic ratio (i.e., horizontal line of the plastic limit) after yielding, spread of plasticity and moment redistribution occurrence. Within the same graphs, the displacement at which collapse occurs is also noted with the vertical dotted lines. The results demonstrate the initially elastic distribution of the bending moments changing to significant redistribution with increasing displacement towards equal moments at collapse.

3. Numerical modelling study

The experimental investigation was supplemented by a numerical modelling investigation which was conducted employing the commercial software package ABAQUS [32]. The developed finite element (FE) models were successfully calibrated based on the material properties of

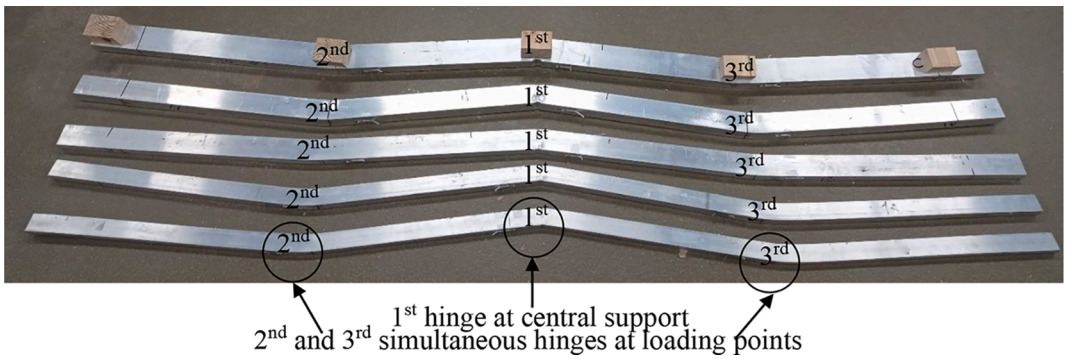

Fig. 16. Failure modes obtained from continuous beam tests.

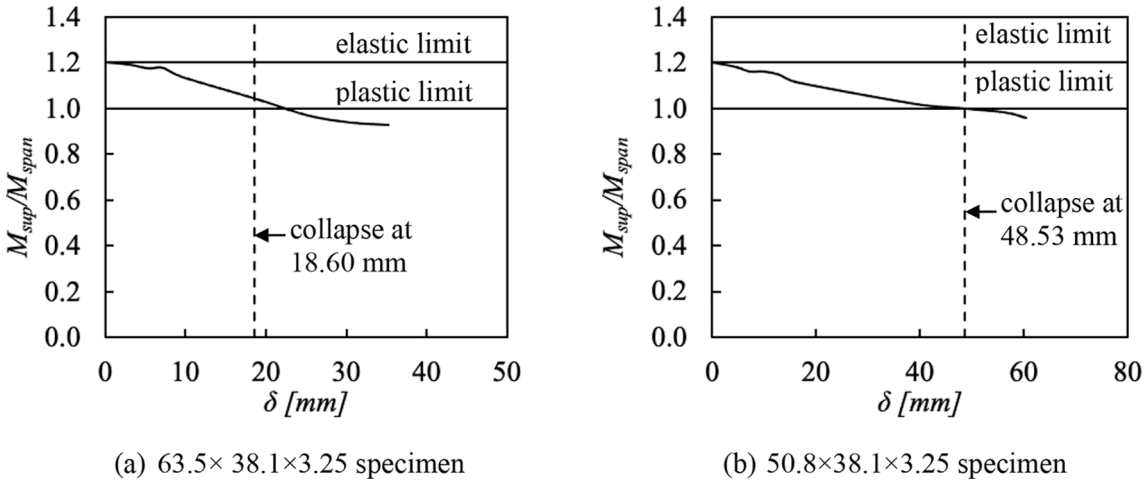

Fig. 17. Evolution of the support to span moment ratio with increasing displacement.

6082-T6 aluminium alloy and validated against the experimental data reported in Section 2. The validated FE models were used for a comprehensive parametric study aimed to extend the pool of performance data for aluminium alloy indeterminate structures. This section presents the adopted modelling assumptions, the accuracy of the validation process and the details of the parametric study.

3.1. Modelling assumptions

Shell elements are commonly employed for the discretisation of thin-walled metallic structural elements, since they are capable of effectively capturing their structural response [14,33–38]. The four-node and doubly curved with reduced integration and finite membrane strains shell element (S4R) was adopted to develop the FE models of this study.

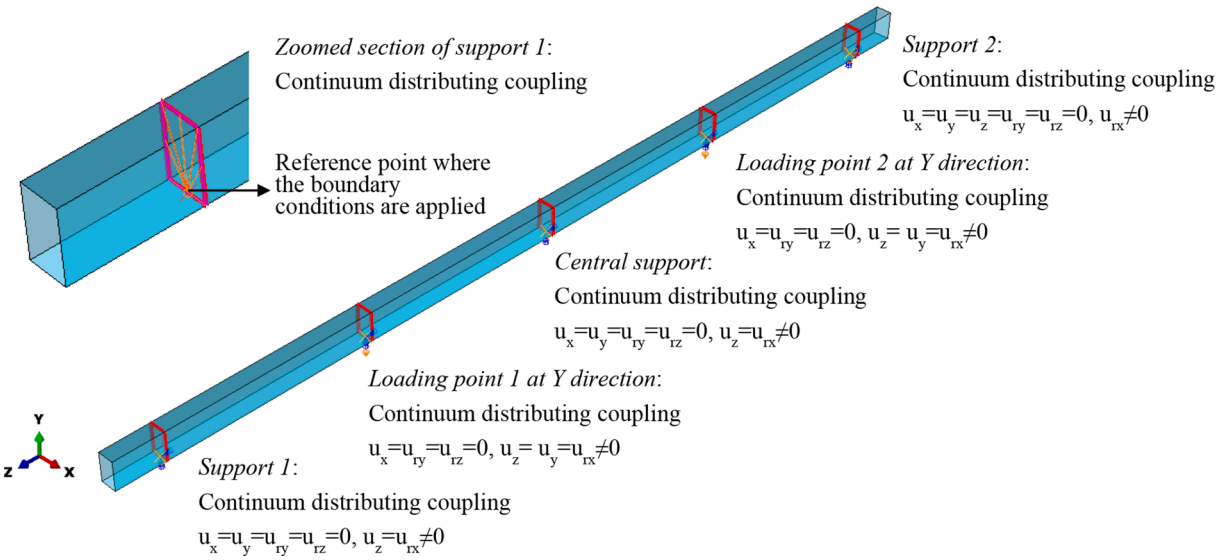

Fig. 18. Modelled geometry of a typical beam specimen and the corresponding applied boundary conditions and constraints.

A mesh convergence study was executed indicating that a uniform mesh with a size equal to the cross-sectional thickness provides reasonable computational time without compromising accuracy. Even though the tests displayed symmetry in geometry, loading and boundary conditions, the full cross-sectional geometric dimensions and length of the examined specimens were modelled. This was chosen so that to include possible antisymmetric local buckling modes which might have slightly lower corresponding eigenvalues than the corresponding symmetric ones [2]. The support and loading conditions were defined in line with the experimental set-ups. To simulate the wooden blocks which were placed to prevent web crippling during testing, distributing coupling constraints were assigned at the supports and loading points (Fig. 18).

The non-linear material behaviour of the examined 6082-T6 aluminium alloy was modelled as elastic–plastic with a von Mises yield criterion and isotropic hardening rule. The measured stress–strain (σ-ε) curves obtained from the tensile coupon tests were utilised in the development of the FE models. Following the ABAQUS [32] requirement for material modelling, the engineering (nominal) stress and strain values were converted to true stress and true plastic strain values.

A linear eigenvalue buckling analysis was performed for each tested specimen to account for the initial local geometric imperfections within the simulations. The lowest elastic buckling mode shape compliant with the observed failure mode was obtained and was incorporated into a subsequent analysis with an amplitude equal to the average measured local imperfection amplitude. It is noteworthy that an additional sensitivity analysis demonstrated a minor effect of the local imperfection amplitude on the flexural response of the aluminium alloy continuous beams, in line with the past studies [15].

The residual stresses caused by the heat-treatment of aluminium alloys were not explicitly incorporated into the simulations [39,40] for the following two reasons. Firstly, the presence of bending residual stresses, which can be reflected by pronounced curving of the tensile coupons [41,42], was not observed herein. Secondly, the residual stresses of extruded aluminium alloy cross-sections have been shown to have a negligible influence on the ultimate strength [43]. Geometrically and materially nonlinear analysis was carried out using the modified Riks solution method to capture each developed FE model's full range flexural response.

Table 5
Comparison of numerical and experimental ultimate loads.

Specimen	$F_{u,FE}/F_{u,Exp}$
Three-point bending	
63.5 × 38.1 × 3.25	1.02
50.8 × 38.1 × 3.25	1.02
50.8 × 25.4 × 3.25	1.00
38.1 × 25.4 × 3.25	1.00
38.1 × 19.1 × 3.25	1.00
Four-point bending	
63.5 × 38.1 × 3.25	1.01
50.8 × 38.1 × 3.25	0.97
50.8 × 25.4 × 3.25	1.00
38.1 × 25.4 × 3.25	1.00
38.1 × 19.1 × 3.25	1.04
Two-span continuous beams	
63.5 × 38.1 × 3.25	1.03
50.8 × 38.1 × 3.25	0.99
50.8 × 25.4 × 3.25	1.04
38.1 × 25.4 × 3.25	1.02
38.1 × 19.1 × 3.25	1.03
mean	1.01
COV	0.02

3.2. Validation of the FE models

Adopting the aforementioned modelling assumptions, the developed FE models were validated by comparing the numerical results with the corresponding experimental ones. To this end, the numerical $F_{u,FE}$ over the experimental $F_{u,Exp}$ ultimate loads for each examined configuration are summarised in Table 5, showing a very good agreement. Typical response curves and failure modes obtained from the experiments and FE models are depicted in Figs. 19 and 20, respectively. As can be observed there is a fairly good agreement between the test and FE results in terms of initial stiffness, ultimate load, post-ultimate behaviour and failure mechanism (1st plastic hinge at the central support and 2nd and 3rd simultaneous hinges at loading points in case of five-point bending). It is worth mentioning that the 50.8 × 25.4 × 3.25 specimen under three-point bending failed by tensile fracture at the bottom flange. This failure pattern was considered within the simulations by monitoring the tensile strains and identifying the point where the developed strains reach the fracture strain ε_f measured from the tensile coupon tests. The numerically and experimentally obtained normalised moment-rotation curves for specimen 50.8 × 25.4 × 3.25 are depicted in Fig. 19(a) and the rhombus signifies the point where the tensile fracture occurred. Overall, it can be considered that the FE models developed herein are capable of accurately replicating the flexural performance of aluminium alloy beams.

3.3. Parametric studies

Following the successful validation of the developed FE models against the experimental results, a series of parametric studies was carried out to generate further data on aluminium alloy two-span continuous beams. The parameters under consideration are summarised in Table 6. Three different aspect ratios D/B were examined, namely 1.0, 1.5 and 2.0, keeping the outer web depth D fixed to 100 mm, whilst the outer flange width B was set equal to 100, 66.7 and 50 mm, respectively. A total of eight cross-sectional thicknesses were studied, extending the experimental results to a broad range of plate slendernesses. Particularly, the slenderness ratio β/ε of the flange (crucial constituent plate element) was ranging from 2.43 to 10.75; where $\beta = b/t$ ($b = B\text{-}2\,t$ is the flat width of the flange under compression and t is the flange thickness) is the slenderness parameter and $\varepsilon = \sqrt{250/\sigma_{0.2}}$ is the material coefficient. Moreover, three aluminium alloy types were considered, namely 6082-T6, 6061-T6 and 6063-T5. The former two alloys represent typical high strength heat-treated aluminium alloys, whilst the latter one represents a typical normal strength aluminium alloy. 6063-T5 aluminium alloy is often referred to as an architectural alloy and offers high corrosion resistance. 6061-T6 aluminium alloy is an American alloy offering medium to high strength and very good corrosion resistance. 6082-T6 is often referred to as a 'structural alloy' and is used predominantly in highly stressed applications such as roof trusses and bridges. For the 6082-T6 alloy, the average material properties obtained from the tensile coupon tests of this study were employed, whilst for the 6061-T6 and 6063-T5 alloys the material properties reported in [15] were adopted. Table 7 lists the material properties of the three aluminium alloys. The two-span continuous beam specimens had 2000 mm overall span length and 100 mm overhang at each end resulting in two equal spans of 900 mm each. Moreover, two loading configurations (LC1 and LC2) were, considered, as shown in Fig. 21. Initial local geometric imperfections were accounted for through the lowest buckling mode shape with an amplitude equal to the average measured local imperfection amplitude. A total of 108 numerical analyses were executed and the obtained results were utilised in the following section to assess the possibility of applying plastic design to aluminium alloy indeterminate structures.

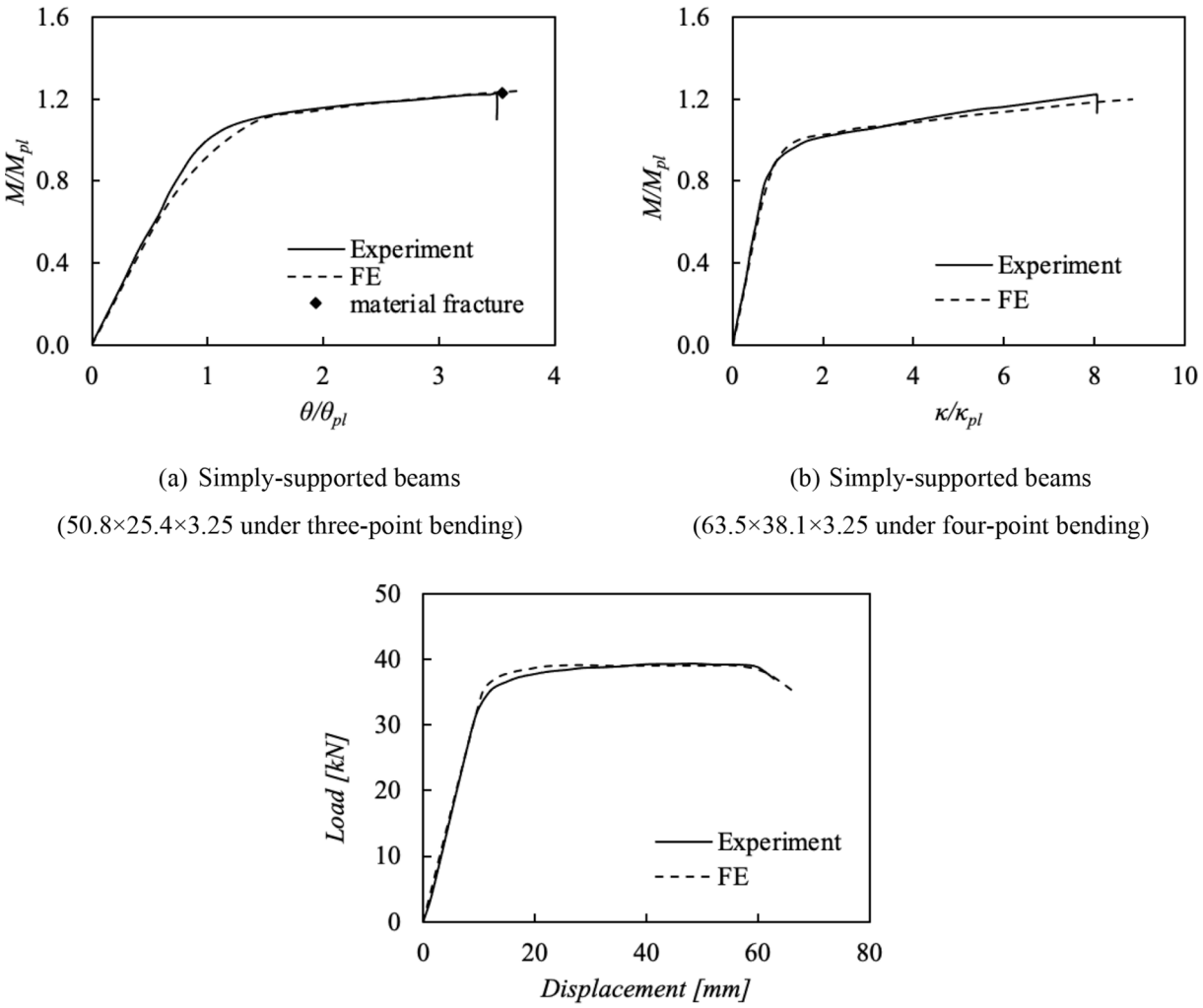

Fig. 19. Comparison between typical numerical and experimental responses.

4. Assessment of design specifications and methods

In this section the experimental and numerical ultimate strengths are utilised to assess the applicability and accuracy of the European design provisions (EC9) [6] and the CSM [44] for single-span simply supported beams (determinate) and two-span continuous beams (indeterminate structures). For the continuous beams the traditional plastic design method is, also, evaluated. Note that all partial safety factors were set equal to unity for these assessments.

4.1. Simply-supported beams

4.1.1. European design provisions

Section 6.2.5 of EC9 [6] provides design criteria for the cross-sectional moment resistance with design values dependent on the classification of the cross-section. It is noted that EC9 [6] adopts a suitable cross-section classification framework to consider the local buckling effect on the cross-sectional structural response. For this reason, slenderness limits for the constituent plate elements are defined, enabling to identify the extent to which the cross-sectional resistance and rotational capacity is limited by the local buckling resistance. Class 1 or ductile cross-sections are capable of developing their collapse resistance without presence of local instabilities. Class 2 or compact cross-sections are capable of developing their plastic moment resistance, whilst their rotational capacity is limited by local instabilities. Class 3 or semi-compact cross-sections are able to reach their elastic moment resistance only since local buckling prevents them from getting into the plastic range. In Class 4 or slender cross-sections the ultimate behaviour is governed by significant local buckling phenomena and failure occurs before the attainment of the proof (yield) strength.

The experimental moment capacities obtained from the three- and four-point bending tests are utilised herein to assess the current EC9 [6] Class 1 and Class 2 slenderness limits for internal elements in compression. To this end, the experimental ultimate moments $M_{u,Exp}$ were normalised by the corresponding plastic moment resistances M_{pl} and were plotted against the slenderness ratio β/ε (Fig. 22(a)); The same figure also displays the value of the current Class 2 slenderness limit $\beta/\varepsilon = 16$ for the examined 6082-T6 alloy, which is classified as Class A material. It can be seen that all data points are above the unity threshold line and on the left side from the current Class 2 slenderness limit value denoting design safety. For assessing the current Class 1 slenderness limit, the deformation capacity R was plotted against the slenderness ratio β/ε as shown in Fig. 22b. The current slenderness limit for Class 1 cross-sections and material Class A is 11 and is also depicted in the same

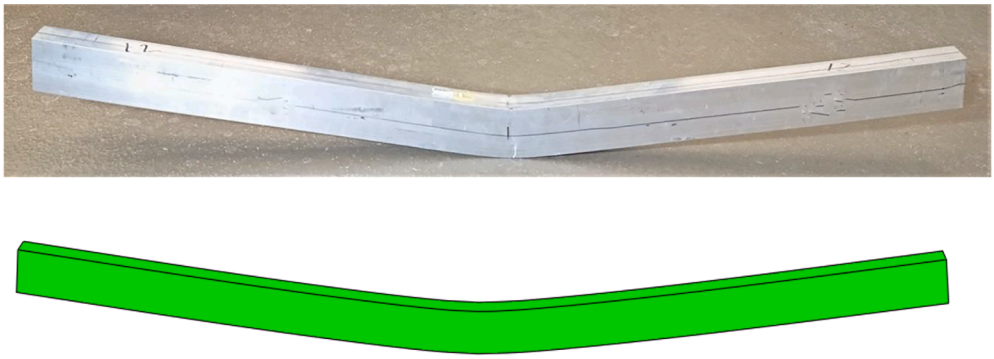

(a) Simply-supported beams (50.8× 25.4×3.25 under three-point bending)

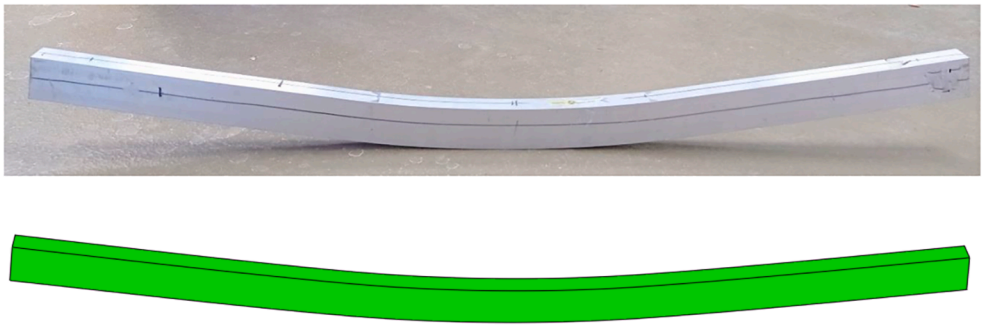

(b) Simply-supported beams (50.8× 25.4×3.25 under four-point bending)

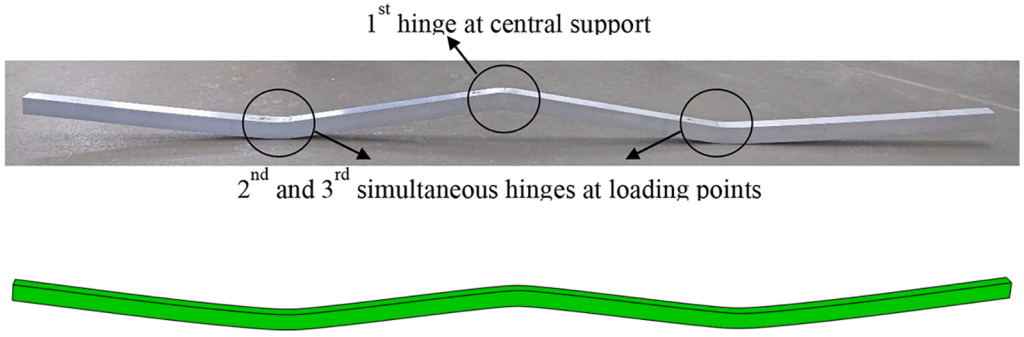

(c) Two-span continuous beams (38.1×25.4×3.25 under five-point bending)

Fig. 20. Comparison between typical numerical and experimental failure modes.

Table 6
List of examined parameters in parametric studies.

	Total FE analyses: 108
3 Aluminium alloys	• 6082-T6 • 6061-T6 • 6063-T5
3 Aspect ratios D/B ($D \times B$) (mm × mm):	• 1.0 (100 × 100) • 1.5 (100 × 66.7) • 2.0 (100 × 50)
8 Plate thicknesses t (mm)	• 5.5, 6, 7, 8, 9, 10, 11, 12 • Resulting slenderness β/ε: 2.43–10.75

Table 7
Material properties for 6082-T6, 6061-T6 [15] and 6063-T5 [15] aluminium alloys adopted in parametric studies.

	E (MPa)	$\sigma_{0.2}$ (MPa)	σ_u (MPa)	ε_u (mm/mm)	ε_f (mm/mm)	n	$\sigma_u/\sigma_{0.2}$
6082-T6	70,302	282	316	0.09	0.14	27.50	1.12
6061-T6	66,000	234	248	0.07	0.10	12.00	1.06
6063-T5	69,000	164	211	0.07	0.14	10.00	1.29

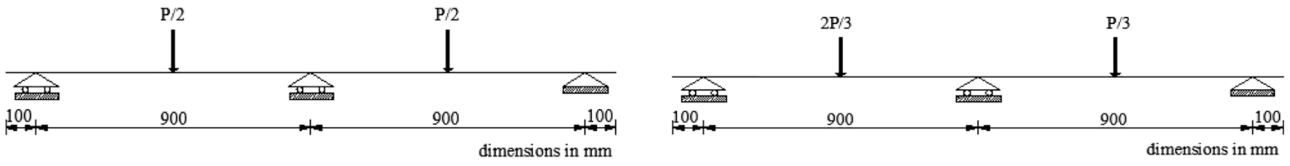

(a) Load configuration 1 (LC1) (b) Load configuration 2 (LC2)

Fig. 21. Load configurations considered in parametric studies.

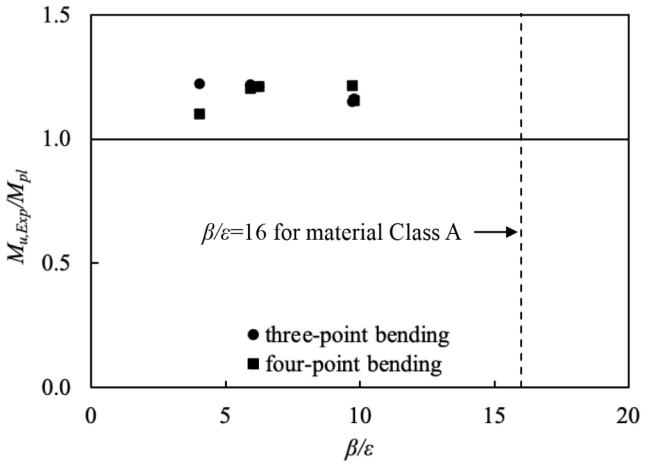

(a) Class 2 slenderness limit

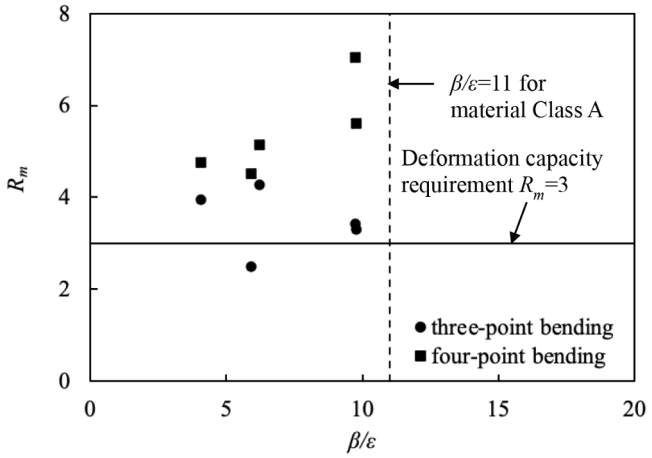

(b) Class 1 slenderness limit

Fig. 22. Assessment of EC9 [6] slenderness limits for internal elements in compression.

figure. Note that there is no specific deformation capacity requirement R for Class 1 cross-sections in EC9 [6] design guidelines. However, Manganiello et al. [19] found that a minimum required value of $R = 3$ adopted from carbon steel is suitable for the case of aluminium alloys. This value is considered in the present study and is included in Fig. 22 (b). As can be observed, all the examined cross-sections exhibited deformation capacity higher than the requirement except from 50.8 × 25.4 × 3.25 specimen which failed by material fracture under three-point bending. Overall, the results denote that the current Class 1 slenderness limit is acceptable.

According to Section 6.2.5 of EC9 [6], the cross-sectional moment resistance M_{EC9} for bending about one principal axis is defined as follows:

$$\mathrm{M}_{EC9} = \alpha_0 W_{el}\sigma_{0.2},\ \alpha_0 = \begin{cases} W_{pl}/W_{el}\ for\ Class\ 1 \\ W_{pl}/W_{el}\ for\ Class\ 2 \\ 1.0\ for\ Class\ 3 \\ W_{eff}/W_{el}\ for\ Class\ 4 \end{cases} \quad (6)$$

where a_0 is the shape factor, W_{pl} is the plastic section modulus of the gross cross-section, W_{el} is the elastic section modulus of the gross cross-section and W_{eff} is the effective elastic section modulus of the cross-section calculated using a reduced thickness for treatment of local buckling.

Despite the considerable effect of material nonlinearity, i.e., strain hardening, on the structural response of Class 1 cross-sections, there is no distinct difference in Equation (6) for the treatment of Class 1 and Class 2 cross-sections. Thus, EC9 [6] includes an alternative method in Annex F for a more accurate evaluation of the moment resistance of Class 1 cross-sections using a correction factor $\alpha_{M,j}$ to consider material strain hardening.

$$\mathrm{M}_{EC9-F} = a_{M,1} W_{el}\sigma_{0.2} \quad (7)$$

$$a_{M,1} = \begin{cases} \alpha_5 = 5 - \dfrac{3.89 + 0.00190n}{a_0^{0.27+0.0014n}},\ 4\% \leqslant \varepsilon_u < 8\%\ (brittle\ alloys) \\ \alpha_{10} = a_0^{[0.21log(1000n)]} 10^{[0.0796-0.0809log(n/10)]},\ \varepsilon_u \geqslant 8\%\ (ductile\ alloys) \end{cases} \quad (8)$$

where α_5 and α_{10} are generalised shape factors depending on the ductility of the aluminium alloy as described in Annex G [6] and n is the strain hardening exponent.

Table 8 presents for each tested cross-section the ratios of the moment resistance according to Section 6.2.5 of EC9 [6] M_{EC9} and Annex F $M_{EC9\text{-}F}$ over the experimentally obtained bending moment capacity $M_{u,Exp}$ under both test configurations. As can be seen, EC9 predictions appear to be safe as both mean values of the $M_{EC9}/M_{u,Exp}$ and

Table 8
Assessment of EC9 [6] and CSM design predictions for simply-supported beams.

Specimen	β/ε	$M_{EC9}/M_{u,Exp}$	$M_{EC9\text{-}F}/M_{u,Exp}$	$\bar{\lambda}_{cs}$	$M_{CSM}/M_{u,Exp}$
Three-point bending					
63.5 × 38.1 × 3.25	9.73	0.87	0.94	0.30	0.96
50.8 × 38.1 × 3.25	9.78	0.86	0.94	0.31	0.93
50.8 × 25.4 × 3.25	5.92	0.82	0.90	0.21	0.91
38.1 × 25.4 × 3.25	6.23	0.83	0.90	0.21	0.90
38.1 × 19.1 × 3.25	4.05	0.82	0.89	0.15	0.89
Four-point bending					
63.5 × 38.1 × 3.25	9.73	0.82	0.89	0.30	0.91
50.8 × 38.1 × 3.25	9.78	0.87	0.95	0.31	0.94
50.8 × 25.4 × 3.25	5.92	0.83	0.91	0.21	0.92
38.1 × 25.4 × 3.25	6.23	0.83	0.90	0.21	0.90
38.1 × 19.1 × 3.25	4.05	0.91	0.99	0.15	0.99
Mean		0.85	0.92		0.92
COV		0.03	0.03		0.03

$M_{EC9\text{-}F}/M_{u,Exp}$ ratios are lower than unity. Moreover, the resulting low coefficients of variation (COVs) denote low scatter and thereby high design consistency. The moment resistances $M_{EC9\text{-}F}$ were found to be more accurate, i.e., closer to unity, than the corresponding M_{EC9} ones, since Annex F accounts for material strain hardening within the calculations.

4.1.2. CSM for determinate structures

The CSM is a deformation-based design method rationally accounting for the influence of material strain hardening exhibited by stocky and slender cross-sections. CSM was originally devised for stainless steel and carbon steel stocky cross-sections [21,45–48]. In subsequent research studies [44,49], the design equations were modified to apply to aluminium alloys covering also the case of slender cross-sections. This method uses an experimentally derived base curve (Fig. 23(a)) to define the maximum attainable strain ε_{CSM} of a cross-section depending on its cross-sectional slenderness $\bar{\lambda}_{cs}$. This base curve is described by the following equations:

$$\frac{\varepsilon_{CSM}}{\varepsilon_{0.2}} = \frac{0.25}{(\bar{\lambda}_{cs})^{3.6}} \leqslant min(15, \frac{0.5\varepsilon_u}{\varepsilon_{0.2}}) \; for \; \bar{\lambda}_{cs} \leqslant 0.68$$
$$\frac{\varepsilon_{CSM}}{\varepsilon_{0.2}} = \left(1 - \frac{0.222}{(\bar{\lambda}_{cs})^{1.05}}\right) \frac{1}{(\bar{\lambda}_{cs})^{1.05}} \; for \; \bar{\lambda}_{cs} > 0.68 \tag{9}$$

where the strain at the ultimate tensile stress ε_u and the cross-sectional slenderness $\bar{\lambda}_{cs}$ are given by the Eqs. (10) and (11), respectively.

$$\varepsilon_u = 0.13(1 - \frac{\sigma_u}{\sigma_{0.2}}) + 0.059 \tag{10}$$

where $\sigma_{0.2}$ is the 0.2 % proof (yield) stress and σ_u is the ultimate tensile stress.

$$\bar{\lambda}_{cs} = \sqrt{\sigma_{0.2}/\sigma_{cr}} \tag{11}$$

where σ_{cr} is the elastic critical buckling stress of the cross-section which can be determined using either analytical equations [50] or numerical tools, such as CUFSM [51]. In the present study, the elastic critical buckling stress σ_{cr} was calculated using the analytical equations derived from [50].

CSM assumes an elastic-linear hardening model to represent the aluminium alloy stress–strain response, shown in Fig. 23(b). The strain hardening modulus E_{sh} can be calculated by the Equation (12).

$$E_{sh} = \frac{\sigma_u - \sigma_{0.2}}{0.5\varepsilon_u - \varepsilon_{0.2}} \tag{12}$$

Based on the ε_{CSM} and the adopted elastic-linear hardening material behaviour, the cross-sectional bending moment capacity M_{CSM} can be determined as:.

$$M_{CSM} = W_{pl}\sigma_{0.2}\left[1 + \frac{E_{sh}}{E}\frac{W_{el}}{W_{pl}}\left(\frac{\varepsilon_{CSM}}{\varepsilon_{0.2}} - 1\right) - \left(1 - \frac{W_{el}}{W_{pl}}\right) \Big/ \left(\frac{\varepsilon_{CSM}}{\varepsilon_{0.2}}\right)^2\right] for \; \bar{\lambda}_{cs} \leqslant 0.68$$
$$M_{CSM} = \frac{\varepsilon_{CSM}}{\varepsilon_{0.2}} W_{el}\sigma_{0.2} for \; \bar{\lambda}_{cs} > 0.68 \tag{13}$$

where W_{pl} is the plastic section modulus of the gross cross-section, W_{el} is the elastic section modulus of the gross cross-section and E is the modulus of elasticity.

The ratio of the moment resistance M_{CSM} over the experimentally obtained bending moment capacity $M_{u,Exp}$ for each examined cross-section under both test configurations is listed in Table 8. It can be seen that the CSM which rationally accounts for the influence of material strain hardening exhibited by stocky cross-sections provides more accurate design predictions compared to Section 6.2.5 of EC9 [6]. However, the achieved accuracy level of the CSM and Annex F of EC9 [6] is the same since both design methods consider material strain hardening within the calculations.

4.2. Continuous beams

4.2.1. Plastic design concept

According to conventional elastic design, the design collapse load is determined when the first plastic hinge forms in the most heavily stressed cross-section of the structure. Conversely, plastic design exploits the ability of indeterminate structures for bending moment redistribution until a sufficient number of plastic hinges forms and imminent collapse occurs. Plastic design utilises the structure's reserve strength beyond the elastic state and thus allowing the structural members to sustain further loading upon their plastic moment capacity is reached. In elastic design, each structural member must have a design bending moment capacity M_d greater than that obtained from an elastic analysis M^*. Under the design loading, if $M_d = M^*$ for one structural member, the first plastic hinge forms at the design load level along the curve as depicted in Fig. 24. Thus, the cross-section employed in practice is chosen to have $M_d > M^*$, so that the first plastic hinge of the structure occurs at a load level above the design loading. Conversely, plastic

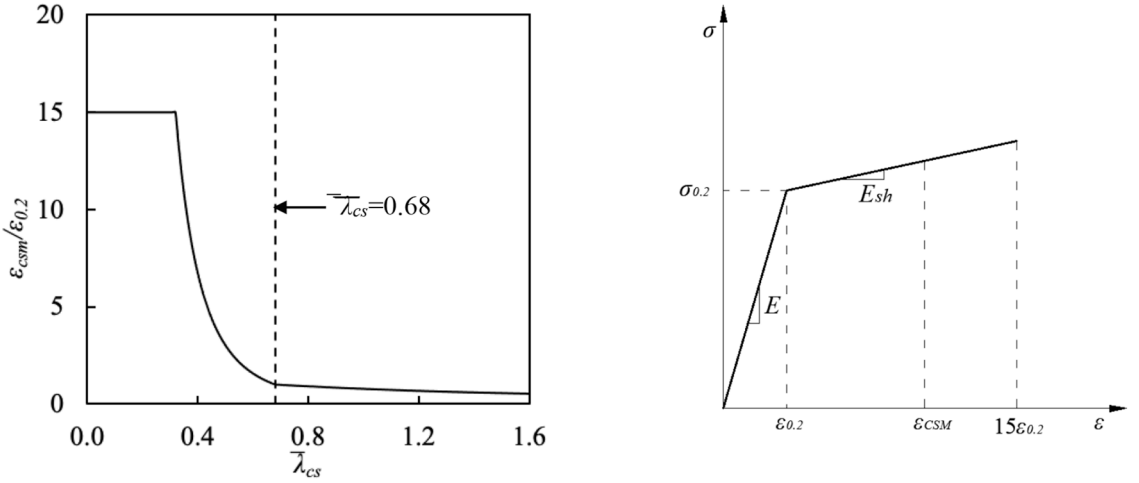

(a) Strain ratio-cross-sectional slenderness curve (b) Elastic-linear hardening material model

Fig. 23. Base curve and material model adopted by CSM [44].

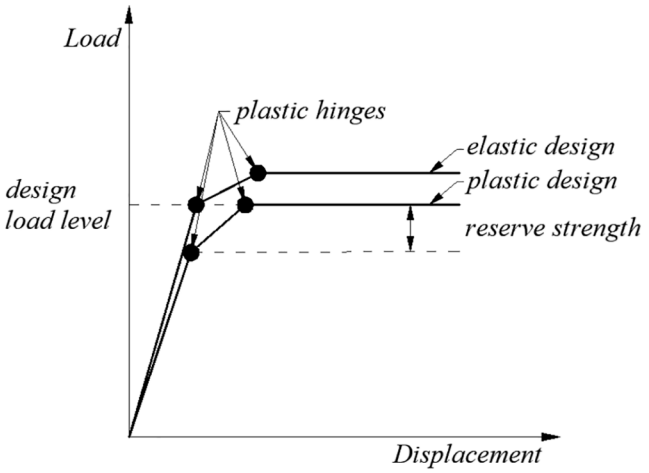

Fig. 24. Comparison between elastic and plastic design concept.

design requires that the last plastic hinge occurs at or above the design load level. Fig. 24 indicates that for the same design loading, the plastic design concept requires a "lighter" structure consisting of components with smaller cross-sections. Thereby, significant material savings can be achieved resulting in a more economically efficient design.

The plastic design may be applied provided that the rotational capacity at the location of the plastic hinges is sufficient to maintain their plastic moment capacity and ability to undergo large inelastic rotations without exhibiting local buckling. Thus, the ductility features of the construction material are one of the key-properties to ensure satisfactory performance and attainment of the plastic collapse load.

4.2.2. Traditional plastic design method

The traditional plastic design method is conventionally employed to indeterminate structures comprising Class 1 cross-sections. This method accounts for moment redistribution and thus the design collapse load corresponds to the load level which causes a collapse mechanism based on the formation of consecutive plastic hinges. Each plastic hinge forms when the most heavily stressed cross-section reaches its plastic moment capacity $M_{tr\text{-}pl\text{-}d}$ which is given by the following Equation:

$$M_{tr-pl-d} = W_{pl}\sigma_{0.2} \tag{14}$$

For simplicity, traditional plastic design idealises the material behaviour adopting an elastic-perfectly plastic stress–strain relationship and thus the additional strength resulting from strain hardening is ignored. Thereby, as far as traditional plastic design method is concerned, the theoretical collapse load ($F_{tr\text{-}pl\text{-}d}$) is expected to be slightly underestimated.

Fig. 25 displays the ratio of the theoretical over the experimentally and numerically obtained strengths $F_{tr\text{-}pl\text{-}d}/F_u$ for both load configurations LC1 and LC2. From this figure, it can be concluded that the traditional plastic design method provides safe but slightly conservative ultimate strengths, i.e., data points below the unity threshold line, particularly for stockier sections. Moreover, it can be observed that the ultimate strengths corresponding to 6082-T6 and 6063-T5 cross-sections appear to be more conservative compared to their 6061-T6 counterparts. This is related to the fact that the traditional plastic design method adopts an elastic-perfectly plastic stress–strain relationship ignoring the material strain hardening behaviour, which is more pronounced in 6082-T6 and 6063-T5 aluminium alloys as shown in Table 7.

4.2.3. European design provisions

EC9 [6] in the main part adopts the elastic global analysis for the design of indeterminate aluminium alloy structures neglecting the ability for moment redistribution at system level due to statical indeterminacy. Thus, the theoretical collapse load is defined when the most

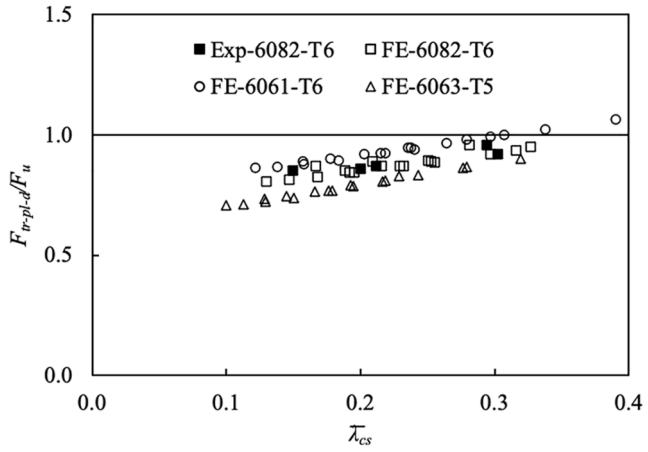

(a) LC1

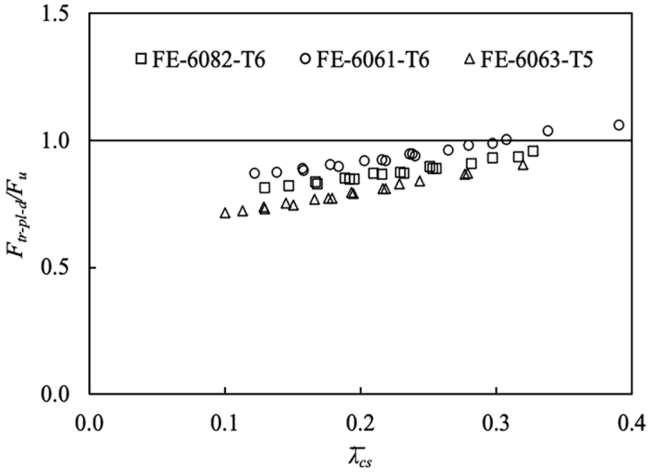

(b) LC2

Fig. 25. Assessment of traditional plastic design method.

heavily stressed cross-section of the structure reaches its bending moment capacity given by Equation (6). However, in ductile indeterminate structures, redistribution of bending moments will occur regardless of whether this was considered or not during the design process. Hence, the structure will fail at a higher loading level than that predicted by the design. Thereby, the global elastic design concept is expected to provide overly conservative design predictions, particularly for aluminium alloy indeterminate structures with stocky cross-sections, i.e., Class 1. To assess this, Fig. 26 presents the ratio of the theoretical over the experimentally and numerically obtained strengths $F_{EC9\text{-}el}/F_u$ for both load configurations LC1 and LC2. As can be seen, all data points are below and far from the unity threshold line, denoting that the global elastic analysis leads to considerably underestimated strength predictions.

However, EC9 [6] is the first international design code which allows plastic design including the plastic hinge method in Annex H. This method applies mainly to Class 1 cross-sections but may be used in Class 2 and Class 3 cross-sections by considering the local buckling effect while determining the ultimate strength. In any case, it should be assured that the structural ductility of the employed aluminium alloy is sufficient for the development of a fully plastic mechanism. The bending moment capacity $M_{EC9\text{-}H}$ according to Annex H of EC9 [6] can be calculated using the Equation (15). The key diversion between the plastic hinge method and the traditional plastic design method is that

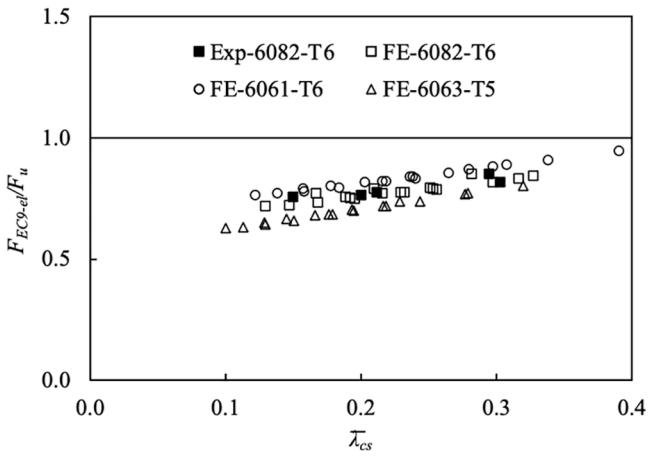

(a) LC1

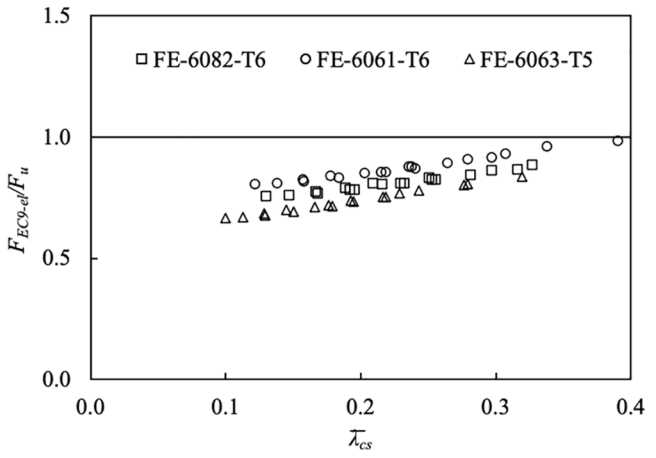

(b) LC2

Fig. 26. Assessment of EC9 [6] using global elastic analysis.

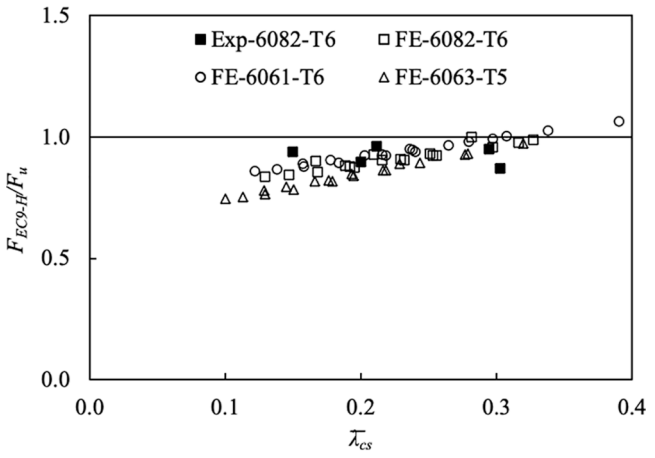

(a) LC1

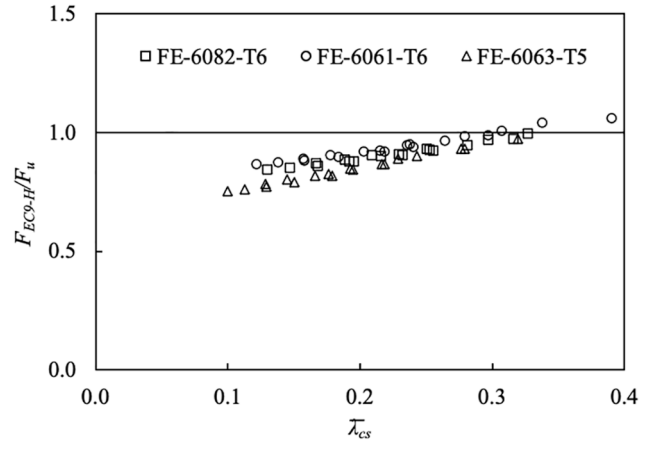

(b) LC2

Fig. 27. Assessment of European design provisions using plastic hinge method from Annex-H [6].

the former considers the beneficial effect of material strain hardening through a correction factor η providing more accurate design provisions.

$$M_{EC9-H} = a_\xi \eta W_{el} \sigma_{0.2} \tag{15}$$

where α_ξ is the shape factor depending on the ductility of the aluminium alloy as described in Annex G [6].

Fig. 27 presents the ratio of the theoretical over the experimentally and numerically obtained strengths $F_{EC9\text{-}H}/F_u$ for both load configurations LC1 and LC2. Upon comparing Figs. 26 and 27, it can be observed that the ratio values in the latter case are closer to unity threshold line denoting that the plastic hinge method results in more accurate and thereby more economically efficient strength predictions. Moreover, the plastic hinge method through the consideration of material strain hardening provides higher level of accuracy than the traditional plastic design method, which approximates the stress–strain response adopting an elastic-perfectly plastic material model (Fig. 25).

4.2.4. CSM for indeterminate structures

The CSM for aluminium alloy determinate structures was extended to cover indeterminate structures [44] adopting merits from the traditional plastic design method allowing for moment redistribution at system level (global plastic analysis). The novelty of this method is that it adopts an elastic-linear hardening material behaviour rather than an elastic-perfectly plastic material behaviour as traditional plastic design method does. Therefore, it accounts for material strain hardening at cross-sectional level resulting in a more accurate estimation of the bending moment capacity. According to CSM, the required rotation at each plastic hinge is different and thus the bending moment capacity differs in each cross-section. As has been mentioned, the CSM is a deformation-based design method evaluating the bending moment capacity based on a strain ratio proportional to the plastic hinge rotational demand. For a given structural configuration, the CSM design collapse load can be determined employing the following summarised steps:

1. Similarly to traditional plastic design method, the location of the i plastic hinges of the considered collapse mechanism and the rotation θ_i for each plastic hinge should be determined.
2. The cross-sectional slenderness $\bar{\lambda}_{cs}$ at each plastic hinge location is calculated using the Equation (11).
3. Based on the CSM base curve, the maximum attainable strain ε_{CSM} at each cross-section is defined employing Equation (9).
4. The rotational plastic hinge demand α_i for each plastic hinge is computed according to Equation (16):

$$\alpha_i = \frac{\theta_i D_i}{(\varepsilon_{CSM}/\varepsilon_{0.2})_i} \tag{16}$$

where D_i is the cross-sectional depth.

The critical (first) plastic hinge is defined as the one which undergoes the highest plastic hinge rotational demand $a_{max} = \max\{\alpha_i\}$ and it is assigned the maximum strain ratio $(\varepsilon_{CSM}/\varepsilon_{0.2})_{\max}$.

5. The strain ratio at each subsequent plastic hinge $(\varepsilon_{CSM}/\varepsilon_{0.2})_{hinge,i}$ is reduced and is calculated in proportion to the rotational hinge demand α_i.

$$\left(\frac{\varepsilon_{CSM}}{\varepsilon_{0.2}}\right)_{hinge,i} = \frac{\alpha_i}{\alpha_{max}}\left(\frac{\varepsilon_{CSM}}{\varepsilon_{0.2}}\right)_{max} \leqslant \left(\frac{\varepsilon_{CSM}}{\varepsilon_{0.2}}\right)_i \tag{17}$$

6. The cross-sectional bending moment capacity m_i at each plastic hinge, is evaluated based on the corresponding strain ratio $(\varepsilon_{CSM}/\varepsilon_y)_{hinge,i}$ using the Equation (17).
7. The theoretical CSM collapse load of the considered structural configuration is determined by equating the external work done by the applied loads F_j through virtual displacements δ_j and the internal work resulting from the rotations θ_i at the plastic hinges.

$$\sum_j F_j\delta_j = \sum_i M_i\theta_i \tag{18}$$

Note that global plastic analysis in CSM should be considered only for a minimum $(\varepsilon_{CSM}/\varepsilon_{0.2})_{\max}$ value of 3.6 for SHS/RHS cross-sections, otherwise elastic global analysis should be employed [44].

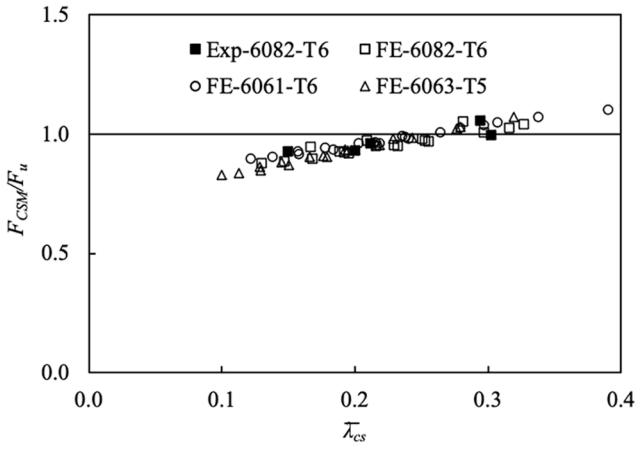

(a) LC1

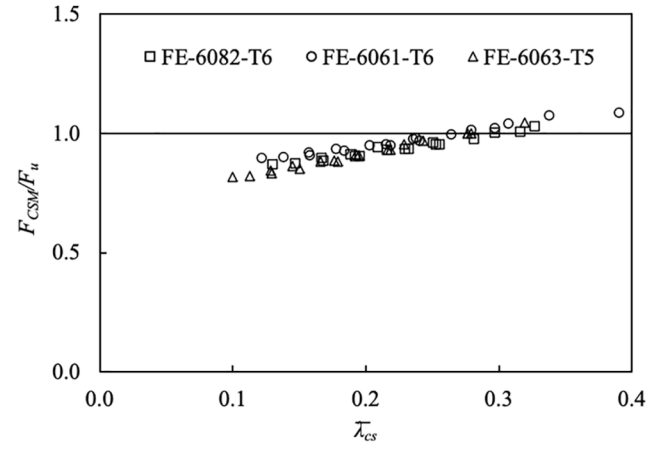

(b) LC2

Fig. 28. Assessment of CSM.

This method is due to lead to improved design predictions owing to the allowance for moment redistribution at system level and the systematic exploitation of material strain hardening at cross-sectional level. To assess this, Fig. 28 presents the ratio of the theoretical over the experimentally and numerically obtained strengths F_{CSM}/F_u for both load configurations LC1 and LC2. As can be seen, the CSM design equations provide accurate strength predictions as all data points are close to the unity threshold line.

4.2.5. Discussion of results

Aiming to evaluate the potential of applying plastic design on aluminium alloy indeterminate structures, this section quantifies the design accuracy and consistency provided by the design methods discussed in the previous sections. For this purpose, the ratios of the theoretical over the experimentally and numerically obtained strengths are summarised in Table 9. The results are also presented separately for the different examined load configurations and aluminium alloys. It can be seen that the application of global elastic analysis, which neglects the ability for moment redistribution at system level provides the most conservative strength predictions, achieving a mean value of the $F_{EC9\text{-}el}/F_u$ ratio equal to 0.79. However, the ultimate loads obtained from the traditional plastic design method, the plastic hinge method of Annex H of EC9 [6] and the CSM provide improved predictions. These methods employ the plastic design concept which utilises the structure's reserve strength beyond the elastic state allowing for higher collapse load than that corresponding to the first yield of the structure. Comparisons amongst these three methods denoted that the traditional plastic design offers the most conservative ultimate loads with a mean value of the $F_{tr\text{-}pl\text{-}d}/F_u$ ratio equal to 0.87. Better accuracy and particularly 14% and 20% is achieved by the plastic hinge method and CSM, which predicted strength ratio with mean values of 0.90 and 0.95, respectively. The improved accuracy owes to the fact that both plastic hinge method and CSM account for the effect of material strain hardening, whilst the traditional plastic design method adopts the approximation of the elastic-perfectly plastic stress–strain relationship. It is noteworthy that the CSM offers slightly more consistent ultimate loads compared to plastic hinge method, achieving the lowest value of COV amongst those resulted from the other design methods. Overall, it can be concluded that plastic design concept and particularly the plastic hinge method included in Annex H of EC9 [6] and CSM can be employed in case of aluminium alloy indeterminate structures providing accurate design strength predictions.

5. Conclusions

This present paper studies the structural performance and design of aluminium alloy indeterminate structures examining the potential of applying the plastic design concept on 6082-T6 aluminium alloy. Five stocky RHS cross-sections made from 6082-T6 heat-treated aluminium alloy were tested as two-span continuous beams to explore the possibility for moment redistribution. The same cross-sections were also subjected to three- and four-point bending tests to quantify their bending moment resistance and rotational capacity. The obtained test data demonstrated the sufficient rotational capacity and capability for moment redistribution of the newly investigated 6082-T6 aluminium alloy. Upon successful validation of the developed FE models, an extensive parametric study was carried out to generate structural performance data for aluminium alloy indeterminate structures. Two load configurations and three heat-treated aluminium alloys, namely 6082-T6, 6061-T6 and 6063-T5, were considered over a wide range of cross-sectional aspect ratios and slendernesses. The experimentally and numerically obtained ultimate strengths were utilised to assess the accuracy and applicability of the traditional plastic design method, the EC9 design provisions, the plastic hinge method included in Annex H of EC9 and the CSM.

The results denoted that the plastic design concept and specifically

Table 9
Assessment of design methods for aluminium alloy continuous beams.

Load configuration	Aluminium alloy	No Exp	No FE	No Exp + FE	$F_{tr\text{-}pl\text{-}d}/F_u$	$F_{EC9\text{-}el}/F_u$	$F_{EC9\text{-}H}/F_u$	F_{CSM}/F_u
LC1	6082-T6	5	18	23	0.88	0.78	0.92	0.96
	6061-T6	–	18	18	0.94	0.83	0.94	0.98
	6063-T5	–	18	18	0.79	0.70	0.84	0.93
LC2	6082-T6	–	18	18	0.87	0.81	0.91	0.94
	6061-T6	–	18	18	0.94	0.87	0.94	0.97
	6063-T5	–	18	18	0.79	0.73	0.84	0.91
Mean	All	5	108	113	0.87	0.79	0.90	0.95
COV					0.09	0.09	0.08	0.07

the plastic hinge method and CSM are suitable for the design of aluminium alloy indeterminate structures. These two design methods address sufficiently the issue of strain hardening at cross-sectional level and moment redistribution at system level resulting in accurate strength predictions. Particularly, the plastic hinge method and CSM provided predicted strength ratio with mean values of 0.90 and 0.95, respectively, which are 14% and 20% more accurate of the corresponding one resulted from global elastic analysis. This study fundamentally extends the pool of performance data for aluminium alloy indeterminate structures by reporting for the first time research results for the relatively new 6082-T6 aluminium alloy along with a detailed numerical study for the already investigated 6061-T6 and 6063-T5 aluminium alloys. Overall, it is concluded that utilising the structure's reserve strength beyond the elastic state allows for higher collapse loads and thereby the full utilisation of the potential of aluminium alloys as a structural material.

Declaration of Competing Interest

The authors declare that they have no known competing financial interests or personal relationships that could have appeared to influence the work reported in this paper.

Acknowledgements

The authors are grateful to the technicians of the School of Civil Engineering and Built Environment and the School of Engineering at Liverpool John Moores University for their valuable assistance. Also, the financial support of the Faculty of Engineering and Technology of Liverpool John Moores University is gratefully acknowledged.

References

[1] Nethercot DA, Li TQ, Choo BS. Required rotations and moment redistribution for composite frames and continuous beams. J Constr Steel Res 1995;35(2):121–63.
[2] Theofanous M, Saliba N, Zhao O, Gardner L. Ultimate response of stainless steel continuous beams. Thin-Walled Struct 2014;83:115–27.
[3] Gkantou M, Kokosis G, Theofanous M, Dirar S. Plastic design of stainless steel continuous beams. J Constr Steel Res 2019;152:68–80.
[4] The Aluminum Association (AA), Aluminum design manual. Washington, DC, 2020. 2020.
[5] Australian/New Zealand Standard (AS/NZS) Aluminium structures part 1: Limit state design. AS/NZS 1664.1:1997. Standards Australia, Sydney, Australia. 1997.
[6] European Committee for Standarization (EC9). Eurocode 9: Design of aluminium structures. Part 1-1: General structural rules - General structural rules and rules for buildings. BS EN 1999-1-1:2007, CEN:2007. BSI; 2007.
[7] Georgantzia E, Gkantou M, Kamaris GS. Aluminium alloys as structural material: a review of research. Eng Struct 2021;227:111372.
[8] De Matteis G, Moen LA, Langseth M, Landolfo R, Hopperstad OS, Mazzolani FM. Cross-sectional classification for aluminum beams-parametric study. J Struct Eng 2001;127(3):271–9.
[9] Moen LA, De Matteis G, Hopperstad OS, Langseth M, Landolfo R. Rotational capacity of aluminum beams under moment gradient. II: numerical simulations. J Struct Eng 1999;125(8):921–9.
[10] Zhu J-H, Young B. Aluminum alloy tubular columns-Part II: parametric study and design using direct strength method. Thin-Walled Struct 2006;44(9):969–85.
[11] Zhu J-H, Young B. Design of aluminum alloy flexural members using direct strength method. J Struct Eng 2009;135(5):558–66.
[12] Kim Y, Pekz T. Ultimate flexural strength of aluminum sections. Thin-Walled Struct 2010;48:857–65.
[13] Su M-N, Young B, Gardner L. Testing and design of aluminum alloy cross sections in compression. J Struct Eng 2014;140(9).
[14] Su M-N, Young B, Gardner L. Deformation-based design of aluminium alloy beams. Eng Struct 2014;80:339–49.
[15] Su M-N, Young B, Gardner L. Continuous beams of aluminum alloy tubular cross sections. I: Tests and FE model validation. J Struct Eng 2015;141(9).
[16] Su M-N, Young B, Gardner L. Flexural response of aluminium alloy SHS and RHS with internal stiffeners. Eng Struct 2016;121:170–80.
[17] Panlilo F. The theory of limit design applied to magnesium alloy and aluminium alloy structures. R Aerinautical Soc 1947:534–71.
[18] Welo T. Inelastic deformation capacity of flexurally-loaded aluminium alloy structures. Norwegian University of Science and Technology; 1990.
[19] Manganiello M, De Matteis G, Landolfo R. Inelastic flexural strength of aluminium alloys structures. Eng Struct 2006;28(4):593–608.
[20] Su M-N, Young B, Gardner L. Continuous beams of aluminum alloy tubular cross sections. II: Parametric study and design. J Struct Eng 2015;141(9).
[21] Gardner L, Wang F, Liew A. Influence of strain hardening on the behavior and design of steel structures. Int Joural Struct Stab Dyn 2011;11(5):855–75.
[22] European Committee for Standardization (CEN). Metallic Materials – Tensile Testing – Part 1: Method Of Test At Room Temperature. Brussels; 2009.
[23] Ramberg W, Osgood WR. Description of stress-strain curves by three parameters. Vol. Technical. Washington, D.C.: National Advisory Committe for Aeronautics; 1943.
[24] Hill HN, Clark JW, Brungraber RJ. Design of welded aluminum structures. J Struct Div ASCE 1960;86(6):101–24.
[25] Theofanous M, Liew A, Gardner L. Experimental study of stainless steel angles and channels in bending. Structures 2015;4:80–90.
[26] Theofanous M, Saliba N, Zhao O, Gardner L, Liew A, Gardner L, et al. Bending strength of hot-rolled elliptical hollow sections. J Struct Eng 2016;125(9):97–109.
[27] Wang J, Afshan S, Gkantou M, Theofanous M, Baniotopoulos C, Gardner L. Flexural behaviour of hot-finished high strength steel square and rectangular hollow sections. J Constr Steel Res 2016;121:97–109.
[28] Ricles JM, Sause R, Green PS, Kuhlmann U. Definition of flange slenderness limits on the basis of rotation capacity values. J Constr Steel Res 1989;0296(97):323–35.
[29] Ricles JM, Sause R, Green PS. High-strength steel: implications of material and geometric characteristics on inelastic flexural behavior. Eng Struct 1998;0296(97):323–35.
[30] Lay MG, Galambos TV. Inelastic steel beams under uniform moment. J Struct Div 1965;91(6):67–93.
[31] Lay MG, Galambos TV. Inelastic beams under moment gradient. J Struct Div 1967;93(1):381–99.
[32] Hibbit, Karlsson, Sorensen. ABAQUS: Theory Manual. Providence, RI (USA): Dassault Systemes Corporation; 2018.
[33] Gkantou M, Theofanous M, Baniotopoulos C. Plastic design of hot-finished high strength steel continuous beams. Thin-Walled Struct 2018;133:85–95.
[34] Zhou F, Young B. Aluminum tubular sections subjected to web crippling-Part I: Tests and finite element analysis. Thin-Walled Struct 2008;46(4):339–51.
[35] Zhu J-H, Young B. Numerical investigation and design of aluminum alloy circular hollow section columns. Thin-Walled Struct 2008;46:1437–49.
[36] Georgantzia E, Gkantou M, Kamaris GS. Numerical modelling and design of aluminium alloy angles under uniform compression. Civil Eng 2021;2(3):632–51.
[37] Georgantzia E, Gkantou M, Kamaris GS, Kansara K, Hashim K. Aluminium alloy cross-sections under uniaxial bending and compression: a numerical study. IOP Conf Ser Mater Sci Eng 2021;1058:012011.
[38] Gkantou M. Numerical study of aluminium alloy square hollow section columns. In: 3rd International Conference on Trends and Recent Advances in Civil Engineering. Uttar Pradesh, Noida, India; 709–17.
[39] Feng R, Liu J. Numerical investigation and design of perforated aluminium alloy SHS and RHS columns. Eng Struct 2019;199.
[40] Wang F, Young B, Gardner L. Thin-Walled Structures Compressive testing and numerical modelling of concrete-filled double skin CHS with austenitic stainless steel outer tubes. Thin Walled Struct 2019;141:345–59.
[41] Rasmussen KJR, Hancock GJ. Design of thin-walled plain channel section columns against flexural buckling. Thin-Walled Struct 1994;20(1–4):219–40.
[42] Jandera M, Gardner L, Machacek J. Residual stresses in cold-rolled stainless steel hollow sections. 2008;64:1255–63.
[43] Mazzolani FM. Aluminum alloy structures. 2nd ed. London: E& FN Spon; 1995.
[44] Su M-N, Young B, Gardner L. The continuous strength method for the design of aluminium alloy structural elements. Eng Struct 2016;122:338–48.

[45] Gardner L, Ashraf M. Structural design for non-linear metallic materials. Eng Struct 2006;28(6):926–34.
[46] Gardner L. The continuous strength method. Struct Build 2008;161(SB3):127–33.
[47] Gardner L, Theofanous M. Discrete and continuous treatment of local buckling in stainless steel elements. J Constr Steel Res 2008;64:1207–16.
[48] Afshan S, Gardner L. The continuous strength method for structural stainless steel design. Thin Walled Struct 2013;68:42–9.
[49] Su MN, Young B, Gardner L. Testing and design of aluminum alloy cross sections in compression. J Struct Eng ASCE 2014;140(9):04014047.
[50] Seif M, Schafer BW. Local buckling of structural steel shapes. J Constr Steel Res 2010;66(10):1232–47.
[51] Z. Li B.W. Schafer Buckling analysis of cold-formed steel members with general boundary conditions using CUFSM: conventional and constrained finite strip methods 2010 Louis, Missouri, U.S.A.